Geological Society of America
Special Paper 403
2006

$^{40}Ar/^{39}Ar$ thermochronology of the Sulu terrane: Late Triassic exhumation of high- and ultrahigh-pressure rocks and implications for Mesozoic tectonics in East Asia

L.E. Webb*
Department of Earth Sciences, Syracuse University, Syracuse, New York 13244, USA
M.L. Leech*
School of Earth Sciences, Stanford University, Stanford, California 94305, USA
T.N. Yang
Institute of Geology, Chinese Academy of Geological Sciences, Beijing, 100037, China

ABSTRACT

Structural and thermochronological data from the Sulu terrane of eastern China document the exhumation of high-pressure and ultrahigh-pressure (UHP) metamorphic rocks to upper-crustal depths by ca. 206 Ma. $^{40}Ar/^{39}Ar$ ages from K-bearing phases record recrystallization and cooling through amphibolite- and upper greenschist–facies conditions during top-to-the-NW noncoaxial shear and suggest cooling rates on the order of 55 °C/m.y. Integration of the $^{40}Ar/^{39}Ar$ data with U/Pb constraints on the timing of UHP metamorphism yields vertical exhumation rates of >6 mm yr^{-1} from mantle to upper-crustal depths. Qualitative thermal models of metamorphic K-feldspars suggest transient reheating in the Jurassic of a magnitude insufficient to reset mica ages. The Yantai-Qingdao-Wulian fault that currently delineates the boundary between the Yangtze and Sino-Korean cratons was active in the Early Cretaceous as a top-to-the-W extensional detachment fault. The youngest phase of deformation recorded by the $^{40}Ar/^{39}Ar$ data is consistent with mid to Late Cretaceous deformation associated with the Tan-Lu fault. In total, the data reveal that high-pressure and UHP rocks of the Sulu terrane reached and resided at higher structural levels by the end of the Late Triassic relative to the high-pressure and UHP rocks presently exposed in the Dabie Shan. Thus, our $^{40}Ar/^{39}Ar$ data from the Sulu terrane provide the tightest constraints thus far on the timing and rates of exhumation of high-pressure and UHP rocks to upper-crustal depths in the orogen.

Keywords: thermochronology, tectonics, eastern China, exhumation rates, microstructural analysis.

*E-mail, Webb: lewebb@syr.edu. Present address, Leech: Department of Geosciences, San Francisco State University, San Francisco, California 94132, USA.

Webb, L.E., Leech, M.L., and Yang, T.N., 2006, $^{40}Ar/^{39}Ar$ thermochronology of the Sulu terrane: Late Triassic exhumation of high- and ultrahigh-pressure rocks and implications for Mesozoic tectonics in East Asia, *in* Hacker, B.R., McClelland, W.C., and Liou, J.G., eds., Ultrahigh-pressure metamorphism: Deep continental subduction: Geological Society of America Special Paper 403, p. 77–92, doi: 10.1130/2006.2403(04). For permission to copy, contact editing@geosociety.org.

INTRODUCTION

The Sulu ultrahigh-pressure (UHP) metamorphic terrane is part of the Qinling-Dabie-Sulu orogenic belt in east-central China and records a history of profound subduction to, and subsequent exhumation from, mantle depths during Permian–Triassic collision between the Yangtze and Sino-Korean cratons. Metamorphic rocks of Yangtze affinity are known to include the world's most extensive exposures of high-pressure and UHP rocks, and thus offer a prime opportunity to study structural, petrological, geochemical, and isotopic systematics associated with regionally extensive subduction of continental lithosphere. Understanding the subduction-exhumation history of the orogen is complicated by multiple phases of deformation and widespread Late Jurassic–Early Cretaceous plutonism. Based on map relationships, the Sulu and Dabie terranes are separated by ~500 km of apparent sinistral offset along the Tan-Lu fault. The timing and nature of this relationship have been variously proposed to be both a primary feature of the Sino Korean–Yangtze collision (e.g., Yin and Nie, 1993) and a late Mesozoic to Cenozoic feature (e.g., Ratschbacher et al., 2000). To date, the Dabie–Hong'an–Qinling portion of the orogen has been the principal target of geochronological investigations (e.g., Ames et al., 1996; Chavagnac et al., 2001; Hacker et al., 1998, 2000; Li et al., 1993; Ratschbacher et al., 2000, 2003; Rowley et al., 1997; Webb et al., 1999b; Xue et al., 1997), while the Sulu region remained relatively understudied in this context until recently (e.g., Leech et al., this volume; Xu et al., this volume). This paper presents new $^{40}Ar/^{39}Ar$ thermochronologic and structural data from the Sulu terrane. Together, these data constrain the timing and rates of exhumation of the UHP rocks to upper-crustal depths and have further implications for the Mesozoic tectonic evolution of the orogen and East Asia.

GEOLOGY OF THE SHANDONG PENINSULA

Metamorphic rocks with Yangtze-craton affinities comprise the high-pressure and UHP units in the Sulu terrane (Fig. 1). Regional evidence for metamorphic coesite in part defines the UHP unit. High-pressure and UHP eclogite blocks are widespread, though volumetrically minor, in host gneiss, schist, and marble. Blocks of garnet peridotite of meter to kilometer scale are found locally throughout the terrane. Field and petrological evidence demonstrates that lithologies hosting UHP eclogites also record UHP metamorphism with peak conditions of ~4 GPa and 800 °C (e.g., Zhang and Liou, 1998; Ye et al., 2002; Liu et al., 2002, 2004a). Isotopic data suggest that the protoliths of the high-pressure and UHP crustal rocks have Proterozoic ages and were subjected to Middle to Late Triassic UHP metamorphism (e.g., Ames et al., 1996; Enami et al. 1993; Yang et al., 2003; Liu et al., 2004b; Leech et al., this volume) and granulite- to amphibolite-facies retrograde overprinting associated with isothermal decompression and local partial melting (Zhang and Liou, 1998; Wallis et al., 2005).

The high-pressure and UHP units are separated from amphibolite- and granulite-facies metamorphic rocks of the Sino-Korean craton by the Yantai-Qingdao-Wulian fault (Fig. 1). Correlation of the metamorphic rocks northwest of the Yantai-Qingdao-Wulian fault with the Sino-Korean craton was challenged by Faure et al. (2001, 2003) and have been interpreted by other workers as part of the Qinling microcontinent (Ratschbacher et al., this volume). Metamorphic rocks on both sides of the fault are unconformably overlain by Jurassic–Early Cretaceous volcanic and sedimentary cover and are intruded by postcollisional Mesozoic granites. Like the Qinling-Dabie portion of the orogen, Late Jurassic–Early Cretaceous igneous activity in the Shandong Peninsula is associated with ore genesis (e.g., Zhang et al., 2003).

Structural Observations

The high-pressure–UHP rocks of the Sulu terrane are characterized by a generally SE-dipping foliation, SE-plunging stretching lineations, and top-to-the-NW shear sense (Wallis et al., 1999; Webb et al., 2002; Faure et al., 2003; Xu et al., this volume; Fig. 1). The foliation within the UHP gneiss is folded about centimeter- to meter-scale folds with SSW- to ENE-plunging axes. Deformation was accompanied principally by recrystallization under amphibolite-facies conditions. The high-pressure unit displays a strong crenulation cleavage, in which S_2 and L_2 parallel the dominant (S_1, L_1) fabric observed in the UHP unit. Structural variability within the UHP unit includes: (1) top-to-the-S sense of shear and S-plunging stretching lineations in L-S tectonites between Lanshantou and Denshan (vicinity of stop 18; Fig. 1); and (2) both top-to-the-NW and top-to-the-W sense of shear and E- to SE-plunging stretching lineations in the Taolin-Shimen area (vicinity of stop 40; Fig. 1). Top-to-the-SE shear sense was recognized in the high-pressure unit by Faure et al. (2003) and Xu et al. (this volume) and was proposed to represent rare vestiges of deformation during subduction. Overall, the regional structure of the Sulu terrane is strikingly similar to that of Hong'an and Dabie Shan (cf. Hacker et al., 2000; Webb et al., 2001; Faure et al., 2003).

In order to better understand the significance of field observations and to select meaningful samples for $^{40}Ar/^{39}Ar$ analyses, we conducted microstructural studies of oriented samples (Leech et al., 2003; this study). Sample descriptions are summarized in Table 1. Petrographic observations reveal that eclogite bodies displaying mesoscopic deformation fabrics are commonly dominated by symplectite at the microscopic scale, suggesting that static recrystallization occurred after deformation was partitioned into the surrounding host gneisses. Syntectonic plagioclase porphyroblasts in retrogressed mafic schist interlayered within quartzofeldspathic gneiss contain folia of hornblende and rutile that are locally continuous with the external foliation defined by biotite and epidote, implying that the observed fabric developed during retrograde metamorphism

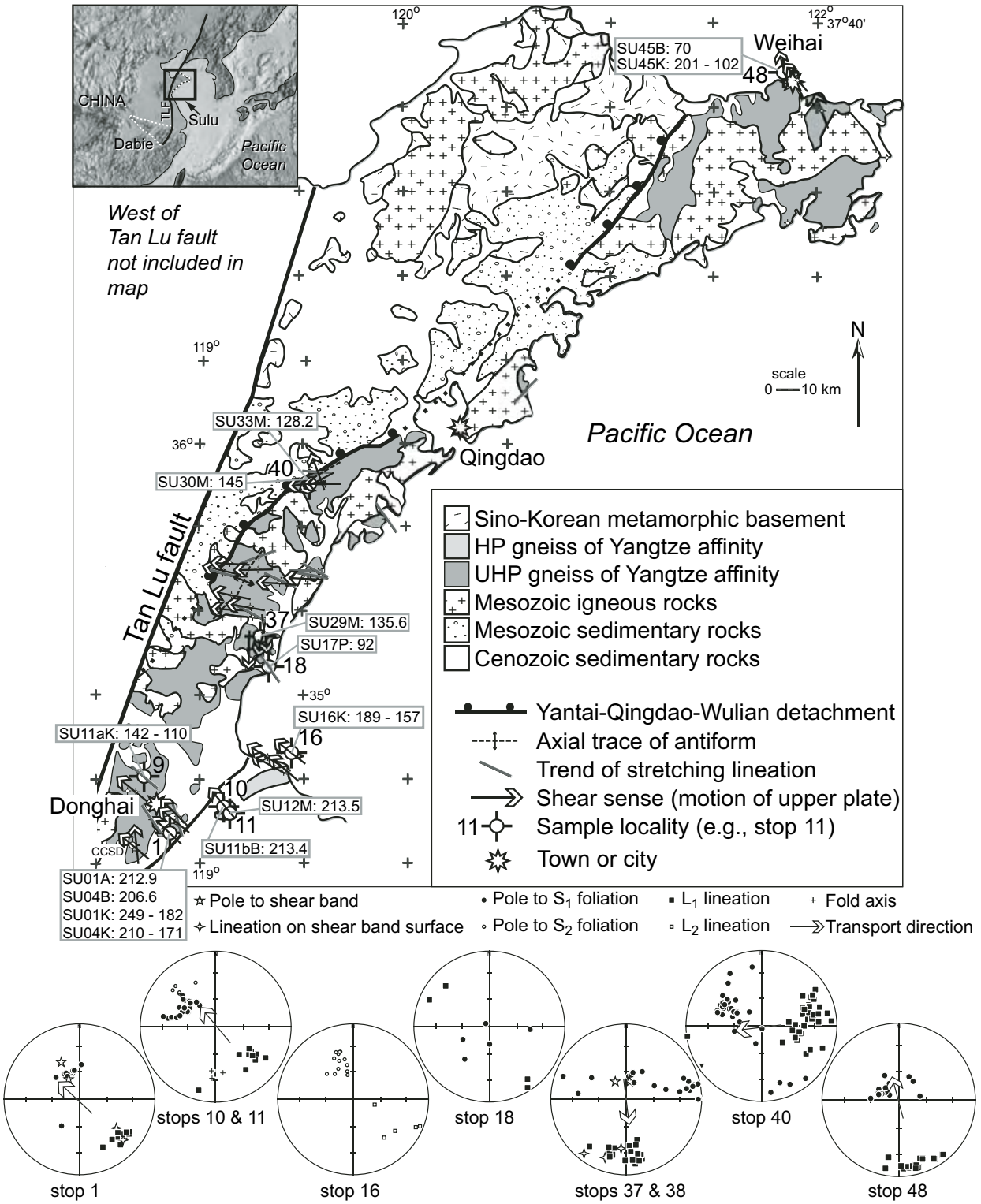

Figure 1. Geologic map of the Sulu terrane in eastern China. Inset shows relative locations of the Sulu terrane and Dabie Shan. TLF—Tan-Lu fault. Map indicates major rock types east of the Tan-Lu fault zone. Results of $^{40}Ar/^{39}Ar$ analyses are indicated with sample localities and are listed in the format of SU01*X: N*, where SU01 is the sample number and *X* corresponds to one of the following abbreviations: A—amphibole; B—biotite; K—K-feldspar; M—white mica; P—pseudotachylite (whole rock). *N* corresponds to the maximum and minimum ages obtained from K-feldspars and the preferred age for all other phases. Structural data collected at sample localities are presented in stereonets with equal-angle, lower-hemisphere projections. Structural data for all other localities visited during this study are summarized by map symbols. Refer to Table 1 to correlate sample numbers with sample localities (stop numbers). HP—high pressure, UHP—ultrahigh-pressure.

from high-pressure to upper greenschist–facies conditions. Polygonized quartz and feldspar lacking undulatory extinction in the core of the NE-trending UHP antiform suggest that at deeper structural levels annealing followed deformation. Greenschist-facies mylonitic fabrics associated with top-to-the-W shear sense are limited to the northwestern limb of the antiform in the vicinity of the Yantai-Qingdao-Wulian detachment fault. We return to a discussion of the timing and significance of these structural observations following presentation of the thermochronologic data.

THERMOCHRONOLOGY OF THE SULU TERRANE

Analytical Procedures

The $^{40}Ar/^{39}Ar$ analyses of samples from the Sulu terrane were performed at the Syracuse University Noble Gas Isotopic Research Laboratory (SUNGIRL). Following sample selection via petrographic analysis, high-purity mineral separates (>99%) were prepared by standard rock-crushing, mineral-separation, and handpicking techniques. After a final acetone wash, mineral separates were wrapped individually in Sn foil and stacked with GA1550 biotite standard (98.79 Ma; Renne et al., 1998), which was used to monitor the neutron dose. Samples were vacuum sealed in a Suprasil quartz tube and irradiated for 10 h in position L-67 of the Ford reactor at the University of Michigan.

The $^{40}Ar/^{39}Ar$ analyses of unknowns were achieved via double-vacuum resistance-furnace heating experiments. Gas was extracted during standard furnace dwell times of 12 min (except for K-feldspar diffusion experiments) and was then exposed for 10 min to hot and cold SAES ST-707 getters for purification. The purified gas was analyzed on a Micromass 5400 mass spectrometer equipped with an electron multiplier.

Sample data were corrected for blanks, mass discrimination, decay of ^{37}Ar and ^{39}Ar, neutron-induced interfering isotopes, and atmospheric argon. Correction factors used to account for interfering nuclear reactions were determined by analyzing argon extracted from irradiated optical grade, fused CaF_2 and K-glass. Correction factors used to account for interfering nuclear reactions for the irradiated samples are: $(^{40}Ar/^{39}Ar)_K = 2.12809 \times 10^{-2} \pm 1.32367 \times 10^{-3}$, $(^{36}Ar/^{37}Ar)_{Ca} = 2.62232 \times 10^{-4} \pm 5.90022 \times 10^{-6}$, $(^{39}Ar/^{37}Ar)_{Ca} = 7.11194 \times 10^{-4} \pm 9.24552 \times 10^{-6}$. All ages were calculated using the decay constants recommended by Steiger and Jäger (1977). Two-sigma analytical errors are reported in this manuscript, unless otherwise noted, and include an error associated with flux monitor age and the irradiation parameter, *J*, typically <1.0% (2σ). Age calculations for inverse isochron and apparent age data were achieved utilizing the program Isoplot 3.0 (Ludwig, 2003). Results of the thermochronologic analyses are summarized in Table 2. Apparent age spectra for samples are shown in Figure 2, with the exception of K-feldspar spectra, shown in Figures 3 and 4 along with multi-diffusion-domain models. Detailed experimental data for all samples are available from the GSA Data Repository.[1]

Geologic Context of Samples and Analytical Results

Below we describe the field, structural, and petrographic observations associated with each sample, because these data are critical to constructing valid interpretations of the thermochronologic data. Discussion of geologic context is followed by analytical results from the step-heating experiments of the respective samples.

Samples SU01 and SU04

Samples SU01 and SU04 come from Fangshan quarry, in the UHP unit southeast of Donghai (stop 1, Fig. 1). Quartzofeldspathic gneiss is the dominant lithology and is intercalated with biotite-rich seams and contains mafic boudins up to several meters in length. Foliation dips moderately to the SSE, and lineations plunge ~30° to the SE. Shear sense is top-to-the-NW, as indicated by amphibole-rich and pegmatitic shear bands, feldspar sigma clasts, and asymmetric boudinage of epidote-amphibolite layers. Field data and petrographic observations both indicate that deformation was synchronous with retrograde amphibolite-facies metamorphism. Thin-section analyses indicate that the dominant recovery mechanism was grain-boundary migration. Partial recovery of quartz and feldspar suggests that either temperature outlasted deformation or that static recrystallization occurred during a younger thermal event (Fig. 5A). Four mineral separates from two samples were dated from this locality: K-feldspar and amphibole from sample SU01, and biotite and K-feldspar from SU04.

SU01 amphibole was sampled from an amphibole-rich seam developed along a shear band surface in quartzofeldspathic gneiss from which the feldspar sample was derived. Step heating resulted in older apparent ages for the first three steps, which account for <1.5% of the cumulative ^{39}Ar released (Fig. 2). The remainder of the experiment produced apparent ages concordant at the 95% confidence interval, with the exception of the 1050 °C step, which was likely associated with in vacuo decomposition of amphibole (Wartho, 1995). The weighted mean age for the forced plateau of 212.9 ± 0.9 Ma is within error of the inverse isochron age defined by the data from the same steps. The inverse isochron defines an intercept within error of a trapped atmospheric component; the error is large because the steps are highly radiogenic.

The age spectrum for SU01 K-feldspar is characterized by ages ranging from 249 Ma to 182 Ma (Fig. 3). The spectrum is characterized by anomalously old ages in the lowest temperature steps, perhaps related to Ar release from adsorption sites or fluid inclusions. This portion of the spectrum is followed by

[1]GSA Data Repository item 2006052, supplementary data tables detailing results of $^{40}Ar/^{39}Ar$ furnace step-heating experiments, is available online at www.geosociety.org/pubs/ft2006.htm, or on request from editing@geosociety.org or Documents Secretary, GSA, P.O. Box 9140, Boulder, CO 80301, USA.

TABLE 1. $^{40}Ar/^{39}Ar$ SAMPLE DESCRIPTIONS

Sample	Locality	Dominant Mineralogy	Relict Phases	Sample Description
SU01	stop 1	Qtz + Pl + Kfs + Am + Bt + Ttn	Grt	QFP gneiss
SU04	stop 1	Qtz + Pl + Kfs + Bt + Ep + opaques	Am, Grt	QFP gneiss
SU11a	stop 9	Qtz + Pl + Kfs + Am + Ep + Ttn		weakly foliated hypabyssal intrusion
SU11b	stop 10	Bt + Pl + Ep + Qtz	Grt, Rt, Am	micaceous shear band
SU12	stop 11	Qtz + Pl + Kfs + Ms + Ep		schist
SU16	stop 16	Qtz + Pl + Kfs + Bt + Ms + Ep + Cal	Am	vein nodule in fold hinge
SU17	stop 18	Glass + Cal + Ser	Qtz , Pl, Kfs	pseudotachylite vein in QFP gneiss
SU29	stop 37	Qtz + Pl + Kfs + Bt + Ep + Ttn	Am, Grt	L-S tectonite
SU30	stop 40	Bt + Qtz + Pl	Phn, Ep, Kfs	micaceous mylonite
SU33	stop 40	Qtz + Kfs + Ms + Pl + Ep		deformed pegmatite
SU45	stop 40	Qtz + Pl + Kfs + Bt	Phn	QFP gneiss

Note: Am—amphibole; Bt—biotite; Cal—calcite; Ep—epidote; Grt—garnet; Kfs—K-feldspar; Ms—muscovite; Phn—phengite; Pl—plagioclase; QFP—quartzofeldspathic; Qtz—quartz; Rt—rutile; Ser—sericite; Ttn—titanite. Note that no chemical data exist for these samples and therefore white mica was inferred to be either muscovite or phengite based on paragenesis and textural relationships observed during microstructural analysis.

TABLE 2. SUMMARY OF RESULTS FOR $^{40}Ar/^{39}Ar$ ANALYSES

Sample	Locality	Phase dated	WMA (Ma)	Analytical error (Ma)	Total error (Ma)	MSWD	$\%^{39}Ar$	N	IIA (Ma)	Error (Ma)	$^{40}Ar/^{36}Ar$ intercept	Error	MSWD	N
SU01	stop 1	amphibole	212.9	1.3	1.7	7.5	98.6	12/17	211.0	2.5	469	330	0.22	12/17
SU04	stop 1	biotite	206.6	1.0	1.4	6.6	91.6	12/17	205.9	1.4	282	6	0.46	17/17
SU11b	stop 10	biotite	213.4	1.2	1.5	7.1	96.7	15/17	212.8	1.4	276	3	1.3	17/17
SU12	stop 11	white mica	213.5	1.4	1.6	11.1	98.4	12/15	214.5	1.5	290	2	1.2	15/15
SU17	stop 18	whole rock	92.1	0.3	1.0	0.52	33.9	4/14	87.7	2.1	3508	230	1.8	8/14
SU29	stop 37	biotite	135.6	0.5	0.9	3.3	88.0	12/16	140.9	3.4	294	13	23	16/16
SU30	stop 40	white mica	159.9	0.6	1.2	2.7	90.5	9/15	155.8	3.4	283	21	7.2	15/15
SU30†	stop 40	white mica	145.3	6.6	6.6	14	7.7	5/15	143.6	9.0	293	39	10.8	5/15
SU33	stop 40	white mica	128.2	0.7	1.3	2.3	82.3	6/13	128.8	1.0	296	2	0.74	13/13
SU45	stop 48	biotite	69.6	2.5	1.4	12	57	4/10	78.0	2.9	262	11	19	9/10

Note: Refer to Table 1 for sample descriptions and to Table 3 for K-feldspar summary. WMA—weighted mean age; MSWD—mean square weighted deviates; $\%^{39}Ar$—percentage of total ^{39}Ar released represented by steps used in WMA calculation; N—number of steps or data points, expressed as a fraction of the total, used in the respective calculation. IIA—inverse isochron age. All errors are reported at the 2σ level. WMA errors include the uncertainty in the irradiation parameter (J factor). Total errors further include uncertainties associated with decay constants.

† Reflects calculations utilizing the subset of data most clearly associated with argon loss.

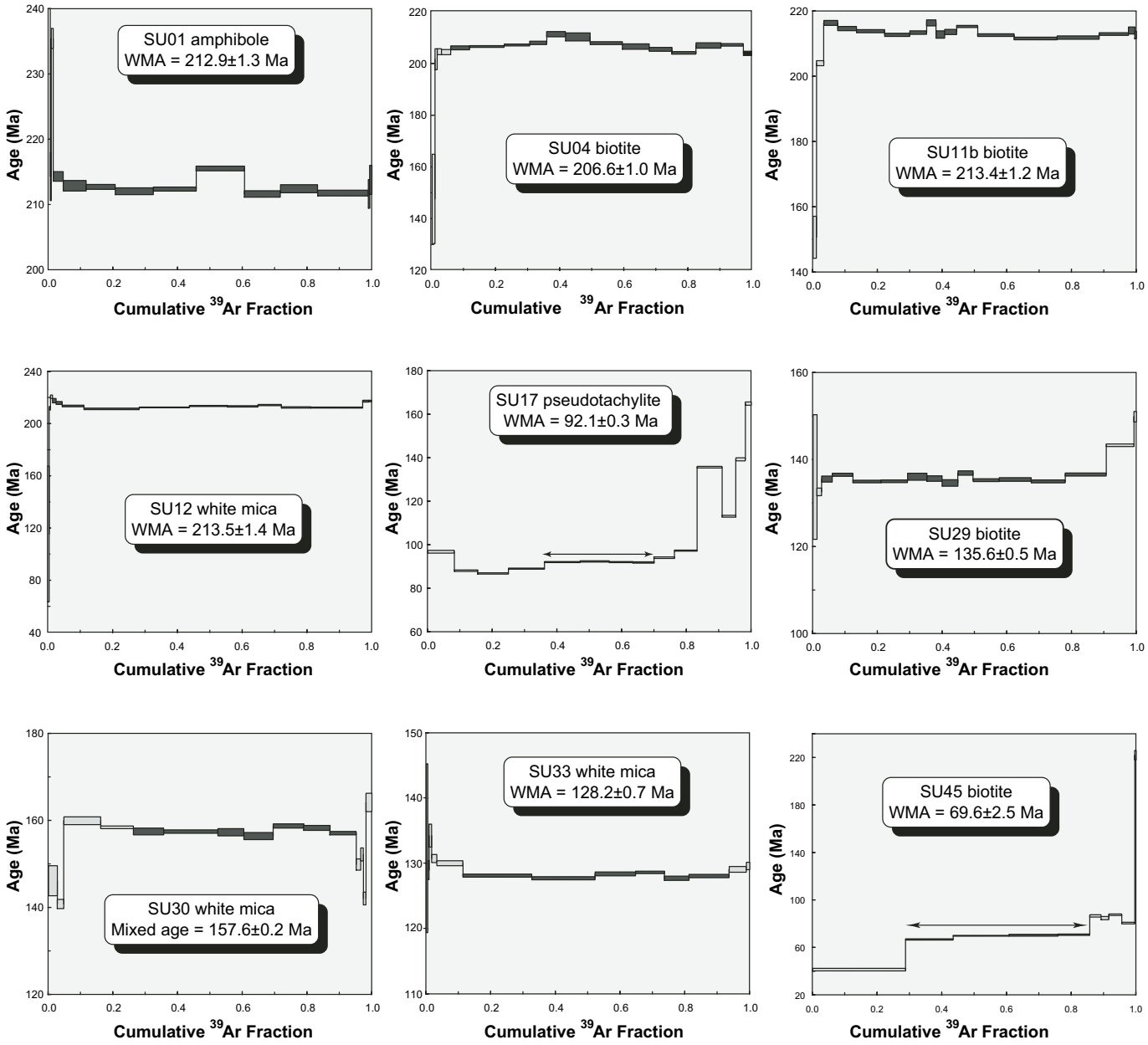

Figure 2. Results of $^{40}Ar/^{39}Ar$ analyses shown with apparent age spectra (see Figs. 3 and 4 for results of K-feldspar analyses); WMA—weighted mean age (forced plateau). Steps included in WMA are filled (or indicated by arrows when scale precludes recognition of filled boxes). Errors indicated in text are 2σ, whereas step ages are 1σ.

three, semiflat apparent age segments at ca. 188 Ma, 232 Ma, and 248 Ma. The isotopic data do not reveal a correlation between K/Ca or K/Cl ratio and age.

Step heating of SU04 biotite resulted in a reasonably flat age spectrum (Fig. 2). Twelve of seventeen steps were selected to calculate the weighted mean age of 206.6 ± 1.0 Ma. The inverse isochron defined a trapped $^{40}Ar/^{36}Ar$ component of 282 ± 6, slightly less than an atmospheric value of 295.5, and an inverse isochron age of 205.9 ± 1.4 Ma. An age of ca. 148 Ma for the first step and the slightly younger ages on the low- and high-temperature end of the steps chosen for the weighted mean age suggest that this sample may have experienced at least one episode of Ar loss, perhaps during the Late Jurassic–Early Cretaceous.

SU04 K-feldspar yielded an apparent age spectrum characterized by maximum and minimum apparent ages of 210 and 171 Ma, respectively (Fig. 3). Four of the five K-feldspar samples dated in this study yielded $^{36}Ar/^{40}Ar$ and $^{39}Ar/^{40}Ar$ isotopic ratios that are clustered rather than correlated. In contrast, the inverse isochron for SU04 K-feldspar is characterized by two discrete

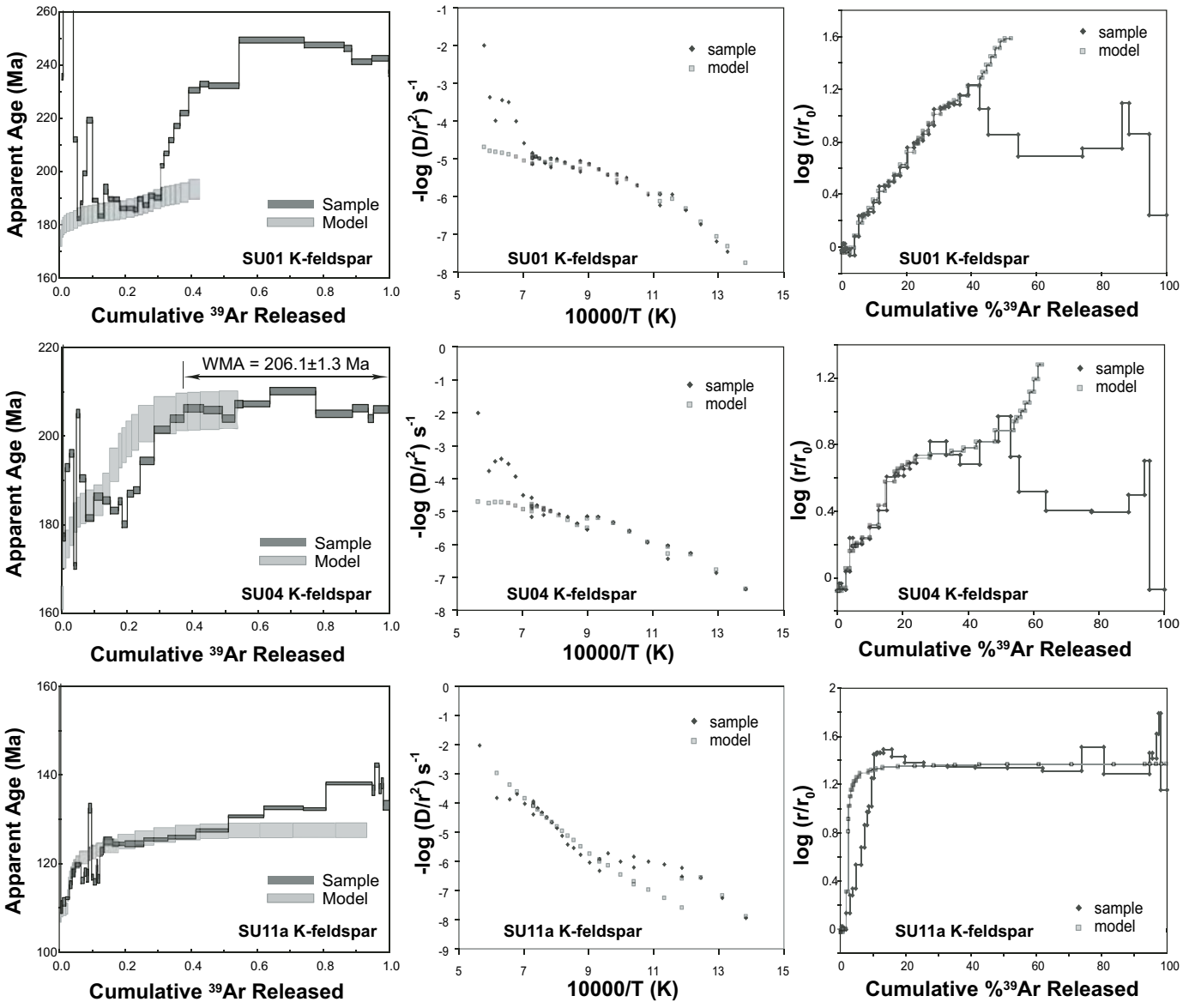

Figure 3. Apparent age spectra and qualitative thermal models for K-feldspar samples SU01, SU04, and SU11a. Step age uncertainties are 1σ. Modeled spectra are shown with 1% age errors. See Figure 7 for best-fit thermal histories associated with modeled spectra.

trends, each defined by data corresponding to temperature steps above and below 1100 °C—the expected breakdown temperature of K-feldspar (e.g., Lovera et al., 1997)—and corresponding to inverse isochron ages of 179 Ma and 204 Ma, respectively (Fig. 6). The isotopic data show no correlation between K/Ca or K/Cl ratios in the data defining the two trends.

Sample SU11a

Sample SU11a, from a weakly deformed hypabyssal intrusion, was sampled from a decimeter-scale outcrop on a hillside within the UHP unit (stop 9, Fig. 1). Within a hundred (covered) meters of the sample location, the lithology changes to quartzo-feldspathic gneisses with SSE-dipping foliation and gently SE-plunging stretching lineations defined by biotite, quartz, and feldspar. Deformation is concentrated in biotite-rich seams, but shear sense was not definitively deduced. In thin section, SU11a is characterized by large equant grains of quartz and feldspar with 120° triple junctions. The foam texture is overprinted by relatively planar zones of reduced grain size and sericitic alteration, accompanied by microcracks and undulatory extinction in neighboring large grains. Sample SU11a K-feldspar produced an apparent age spectrum characterized by maximum and minimum apparent ages of 142 Ma and 110 Ma, respectively (Fig. 3).

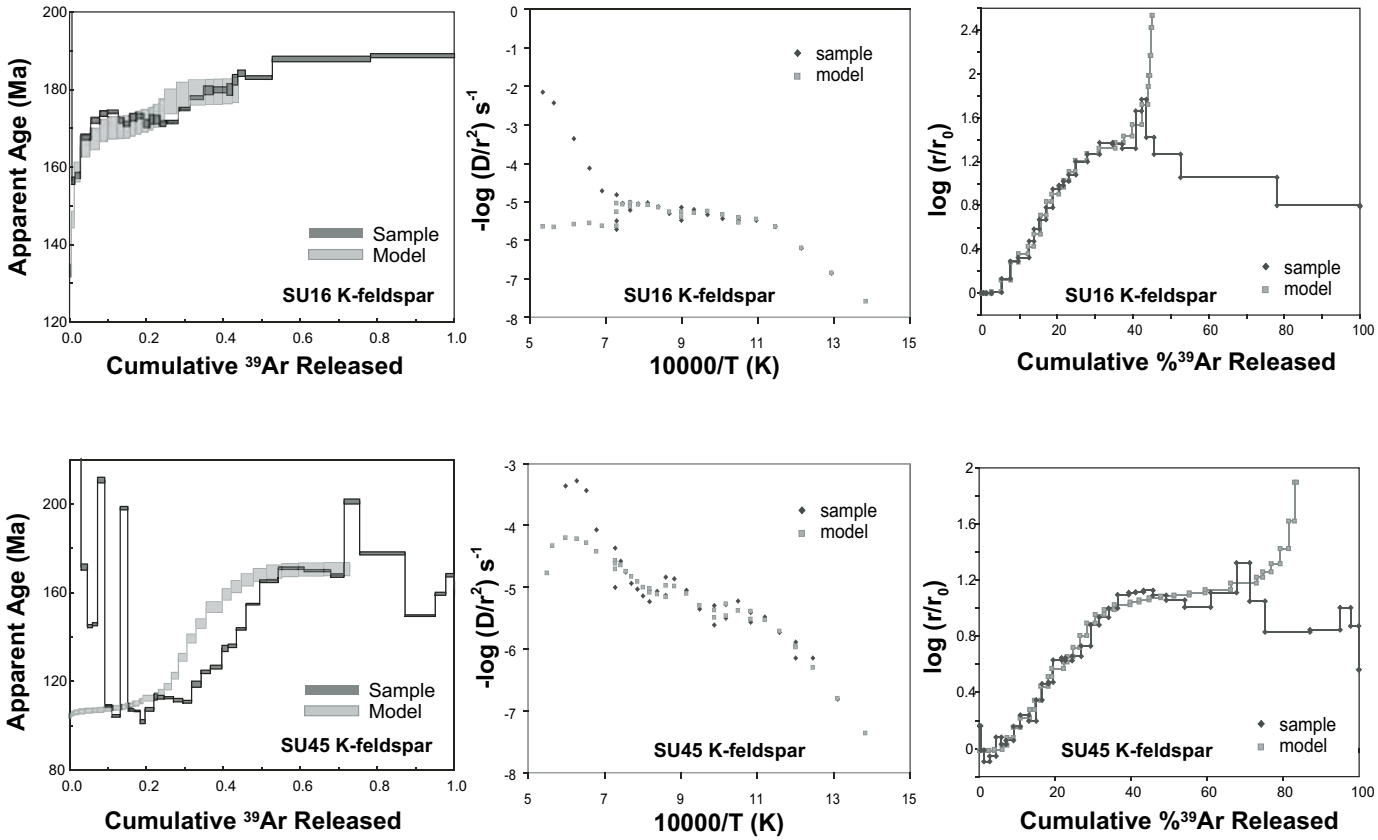

Figure 4. Apparent age spectra and qualitative thermal models for K-feldspar samples SU16 and SU45. Box heights on experimentally derived spectra are shown at 1σ. Modeled spectra are shown with 1% errors on age. See Figure 7 for best-fit thermal histories associated with modeled spectra.

Samples SU11b and SU12

Sample SU11b was taken from a biotite-rich top-to-NW shear band within the Jingping metavolcanic rocks of the high-pressure unit at locality 10, near the village of Paigou (Fig. 1). Sample 12 comes from the metavolcanic rocks at a nearby locality (stop 11). The dominant lithology, white mica–chlorite–albite–quartz schist, is characterized by a strong crenulation cleavage imparted by intense folding. An intersection lineation trends 105–110°. Significantly, S_2 foliations and L_2 stretching lineations defined by micas are essentially identical to those of the UHP unit. This suggests that the dominant S_1 and L_1 fabrics observed in the UHP unit in the Donghai region are likely equivalent to S_2 and L_2 in the high-pressure unit, and that any older fabrics of the UHP unit may have been fully transposed. The biotite-rich shear band displays only the S_2 fabric at mesoscopic scales, yet preserves the S_1 foliation as inclusion trails of rutile and amphibole within plagioclase porphyroblasts (Fig. 5B). Biotite and white mica define L_2 stretching lineations. Field and petrographic observations suggest that the amphibolite–upper greenschist facies overprint was synchronous with S_2 fabric development.

SU11b biotite yielded a weighted mean age of 213.4 ± 1.2 Ma (Fig. 2). The age spectrum suggests some Ar loss, apparent in the first two steps, which comprise <4% of the total ^{39}Ar released; the youngest apparent age is ca. 151 Ma. The inverse isochron, defined by the fifteen steps of the forced plateau, yielded an inverse isochron age of 212.8 ± 1.4 Ma, concordant with the weighted mean age, and a trapped ^{40}Ar/^{36}Ar component with a value of 276, a value less than atmospheric.

SU12 white mica also produced an apparent age spectrum with two younger initial steps that had cumulative ^{39}Ar accounting for ~1% of the total ^{39}Ar released (Fig. 2). The weighted mean age for this sample was 213.5 ± 1.4 Ma, identical to the weighted mean age obtained from sample SU11b. The inverse isochron for SU12, based on twelve of the fifteen total steps, gave an inverse isochron age of 214.5 ± 1.5 Ma and a trapped ^{40}Ar/^{36}Ar component of 290 ± 2, just slightly less than atmospheric.

Sample SU16

SU16 comes from a coastal island quarry within the high-pressure unit (locality 16, Fig. 1). This outcrop bears similarities to other exposures within the high-pressure unit, such as a strong crenulation cleavage and an intersection lineation that trends 110°. An S_1 foliation in felsic rocks is defined by compositional banding of quartzofeldspathic and mica-rich

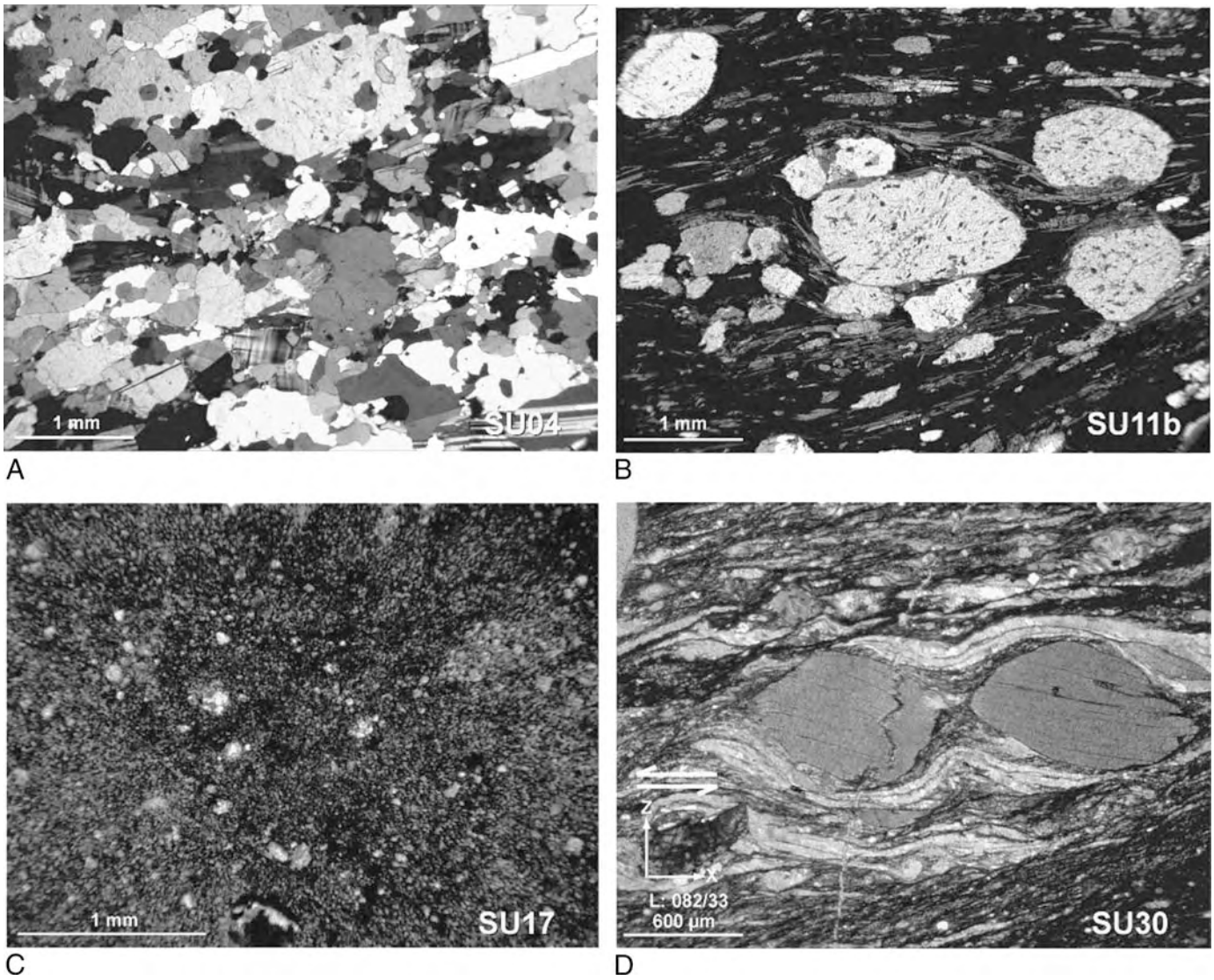

Figure 5. Photomicrographs of Sulu samples. (A) Gneissic texture resulting from recovery of quartz and feldspar in sample SU04 quartzofeldspathic gneiss (crossed polars). (B) Plagioclase porphyroblasts with internal foliation defined principally by rutile and amphibole in sample SU11b mafic schist (plane light). (C) Pseudotachylite sample SU17 is a mixture of glass and cataclasite (crossed polars). (D) Ultramylonite sample SU30 contains dynamically recrystallized quartz and very fine-grained biotite grown at the expense of white mica porphyroclasts (crossed polars). Top-to-the-W shear sense was deduced from both mesoscopic and microscopic features. Sample orientation is normal to the foliation and parallel to the stretching lineation.

domains. An S_2 foliation dips moderately to SSE, and L_2 stretching lineations plunge to the SE. The quartzofeldspathic gneiss contains euhedral chalcopyrite crystals and is host to larger swaths of biotite-epidote-albite seams and boudins. The S_1 and S_2 foliations within the mafic rocks are concordant with those of the host gneiss. Kinematic indicators include asymmetric boudins of quartz veins showing top-to-the-NW sense of shear. At least one episode of fluid infiltration is associated with pegmatitic veins, and nodules of K-feldspar and quartz are concentrated in fold hinges; SU16 comes from one of these nodules.

SU16 K-feldspar produced an age spectrum with maximum and minimum apparent ages of 189 Ma and 157 Ma (Fig. 4). The age spectrum has two apparent flat segments that correspond to ages of ca. 172 Ma and ca. 188 Ma.

Sample SU17

Sample SU17 comes from a hillside quarry, locality 18, within the mapped boundary of the UHP unit (Fig. 1). The dominant rock type is a two-mica amphibolite-grade quartzofeldspathic gneiss with mafic bands rich in epidote and amphibole. A SE-dipping foliation and SE-plunging lineation are heavily

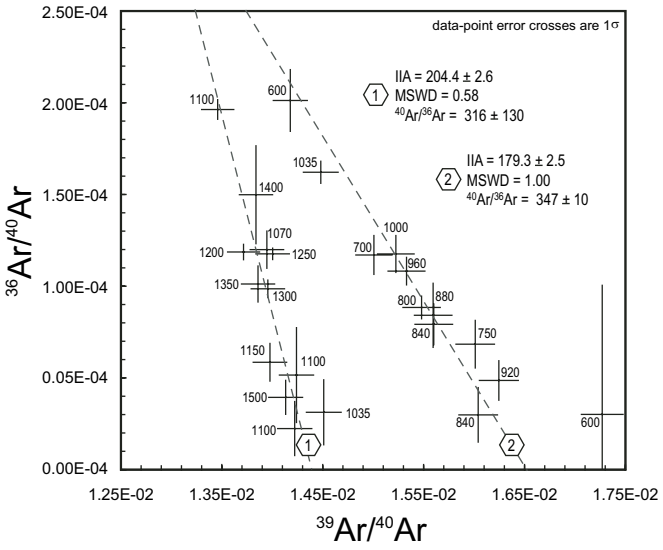

Figure 6. Inverse isochron analysis (IIA) for SU04 K-feldspar shows two discrete trends of data. Data show 1σ errors; adjacent numbers indicate temperature. Only data shown were used in regressions. The oldest age is within error of the weighted mean age (206 Ma) calculated for higher-temperature steps comprising >60% of the ^{39}Ar released (see Fig. 3). MSWD—mean square of weighted deviates.

obscured by chlorite-filled fractures and abundant massive to fine-grained pseudotachylite veins. SU17 is a sample of the pseudotachylite. Petrographic analysis of the pseudotachylite reveals that it is a mixture of glass and cataclasite with rare clasts up to ~100 μm in diameter (Fig. 5C).

Step heating of sample SU17 resulted in a weighted mean age of 92.1 ± 1.3 Ma, calculated utilizing data from our steps in the middle and flattest portion of the spectrum, accounting for 33.9% of the ^{39}Ar released. The spectrum is interpreted as a loss profile resulting from deformation-induced resetting of the Ar systematics of the gneissic protolith at ca. 92 Ma. Eight of the fourteen steps yielded an inverse isochron age of 87.7 ± 2.1 Ma, concordant with the weighted mean age at the 95% confidence level. The trapped ^{40}Ar/^{36}Ar component indicated by the inverse isochron was 3508 ± 230, much greater than atmospheric. This high trapped ^{40}Ar/^{36}Ar value supports the notion that the sample was incompletely reset during deformation, an interpretation supported by both the form of the age spectrum and the petrographic observations.

Sample SU29

Sample SU29 from locality 37 represents a unique structural domain within the mapped boundaries of the UHP unit that is dominated by L-S tectonites (Fig. 1). The rock is quartzofeldspathic gneiss with biotite and intermittent mafic lenses. Foliation is somewhat variable where recognizable and dips steeply WSW or SW. Stretching lineations plunge S and are defined by quartz rods and elongate K-feldspar. Shear sense is top-to-the-S. Thin-section textures indicate dynamic recrystallization of the constituent minerals.

SU29 biotite yielded a weighted mean age of 135.6 ± 0.5 Ma from twelve of sixteen steps, which account for 88% of the total ^{39}Ar released (Fig. 2). The inverse isochron calculated utilizing data from all sixteen steps resulted in an inverse isochron age of 140.9 ± 3.4 and an atmospheric ^{40}Ar/^{36}Ar intercept.

Samples SU30 and SU33

Two samples, SU30 and SU33 were collected from locality 40 along the Yantai-Qingdao-Wulian fault zone (Fig. 1). Rock types at this locality are diverse and include variably retrogressed eclogite blocks in quartzofeldspathic gneiss, abundant and massive pegmatitic veins, and marble (the latter as float). Deformation at greenschist-facies conditions produced foliations with shallow to moderate SW dips and subhorizontal E-W stretching lineations. This deformation is only weakly manifested in the eclogite boudins by vague lineations on boudin margins. Shear sense is top-to-the-W. SU30 is a micaceous ultramylonite that is dominated by white mica porphyroclasts and very fine-grained synkinematic biotite in thin section (Fig. 5D). SU33 is a synkinematic pegmatite vein with white mica. Both samples exhibit dynamically recrystallized quartz.

SU30 white mica produced a hump-shaped spectrum (Fig. 2). The plateau-like segment yielded a weighted mean age of 159.9 ± 0.6 Ma. An inverse isochron generated with all fifteen data resulted in an inverse isochron age of 155.8 ± 3.4 Ma and a ^{40}Ar/^{36}Ar intercept of 283 ± 21. Based on the hump-shaped spectrum and petrographic observations, the weighted mean age is interpreted to be a mixed age as a result of Early Cretaceous Ar loss. A weighted mean age calculated using the youngest apparent ages from the low- and high-temperature steps gave 145.3 ± 6.6 Ma, corresponding to ~8% of the total ^{39}Ar released. The inverse isochron age calculated for these steps resulted in 143.6 ± 9.0 Ma and corresponds to a trapped ^{40}Ar/^{36}Ar ratio of 293, within error of atmospheric.

SU33 white mica resulted in a weighted mean age of 128.2 ± 0.7 Ma based on six steps, which account for 82% of the total ^{39}Ar released. An inverse isochron age of 128.8 ± 1.0 Ma calculated from all 13 data recorded an atmospheric ^{40}Ar/^{36}Ar component.

Sample SU45

SU45 was sampled from an island to the north of Weihai area on the Shandong Peninsula (Fig. 1). Quartzofeldspathic gneiss encapsulates amphibolite boudins up to several meters in length. Foliations dip gently to the ESE, and stretching lineations defined by quartz, feldspar, biotite, and hornblende plunge to the SSE. Asymmetric boudinage of amphibolite layers and feldspar sigma clasts indicate top-to-the-NW shear. The sample shows evidence of late low-temperature deformation in the form of fractures in feldspars and undulatory extinction in quartz, with deformation concentrated along grain boundaries.

SU45 biotite produced an apparent age spectrum with two flat segments followed by a final step that yielded an age of ca. 220 Ma (Fig. 2). A weighted mean age of 69.6 ± 2.5 Ma was

calculated based on the intermediate steps that make up 57% of the total ^{39}Ar released. A short flat segment at high temperature corresponds to an apparent age of ca. 87 Ma. The spectrum is interpreted to reflect Ar loss associated with the low-temperature deformation observed in thin section. An inverse isochron calculated using the four steps associated with the weighted mean age yielded an inverse isochron age of 78.0 ± 2.9 Ma and a $^{40}Ar/^{36}Ar$ intercept of 262 ± 11.

SU45 K-feldspar yielded an apparent age spectrum with a steep profile (Fig. 4), which, neglecting steps with anomalously old ages in the first 15% of the ^{39}Ar released, is characterized by minimum and maximum ages of 102 and 201 Ma. The shape of the spectrum further indicates that the K-feldspar exhibited anomalous degassing behavior during the experiment at temperatures >1100 °C.

K-Feldspar Multi-Diffusion-Domain Models

The thermal histories of five K-feldspar samples were explored via the multi-diffusion-domain modeling (MDD) techniques of Lovera et al. (1989; http://sims.ess.ucla.edu/argon.htm). We refer the reader to McDougall and Harrison (1999) and Parsons et al. (1999) for detailed discussions and debates on the application and viability of MDD modeling. Model parameters were determined by modeling the experimental Arrhenius data with the program AUTOARR (Figs. 3 and 4; Table 3). All samples, with the exception of SU11a, yielded reasonably good fits to the experimentally derived diffusion data for temperatures <1100 °C, where onset of melting of K-feldspar typically commences and loss via volume diffusion ceases (McDougall and Harrison, 1999; Figs. 3 and 4). The poor fits for sample SU11a were most likely a result of the late brittle deformation seen in the microstructures. Sample SU45 also showed evidence for late brittle deformation. Activation energies determined for the metamorphic feldspars (i.e., all except for SU11a) were 30–38 kcal mol^{-1}, on the low end of the activation energies typical for K-feldspars from crystalline rocks (Lovera et al., 1997; Table 3).

The complex nature of apparent age spectra for all samples (e.g., multiple ramp-flat features as opposed to serially increasing ages, anomalous degassing behavior) indicates that the samples may be complicated by deformation-related Ar loss and/or low-temperature recrystallization, therefore precluding rigorous interpretation of the MDD models (Lovera et al., 2002). However, to place qualitative constraints on the time of cooling below ~300 °C, the apparent age spectra were modeled manually via the program AGESME. Various thermal histories were explored (e.g., monotonic cooling, isothermal holding, and transient reheating), taking into account independent temperature-time constraints from step-heating experiments described already and from other isotopic systems employed in our study (cf. Leech et al., this volume). Figure 7 presents the thermal histories that yielded the best model fits to the experimental age spectra obtained for each of the samples (see Figs. 3 and 4 for experimental and model spectra). Because these models allow reheating, they are nonunique solutions, and we emphasize that the models are only qualitative assessments of possible thermal histories of these K-feldspars. Next we discuss the interpretations associated with the MDD models in conjunction with the geologic constraints and the thermochronological data detailed previously.

DISCUSSION

The combined thermochronologic, structural, and petrographic data have implications for the Triassic exhumation history of the high-pressure–UHP rocks as well as for later Mesozoic tectonic events in East Asia. Fifteen $^{40}Ar/^{39}Ar$ step-heating analyses revealed information regarding what appear to be distinct tectonic events in the Sulu region: Late Triassic exhumation following peak metamorphism, Late Jurassic–Early Cretaceous igneous activity and detachment faulting, and mid to Late Cretaceous brittle faulting (Fig. 7). Qualitative MDD models of K-feldspar suggest the possibility of at least one, and possibly two, thermal excursions during Jurassic time (Fig. 7).

Late Triassic Exhumation to Upper-Crustal Depths

Field observations and microstructural data support an interpretation that the cluster of ages ca. 213 Ma corresponds to recrystallization at amphibolite- to upper greenschist–facies conditions. Field and microstructural evidence indicate that at that time, the UHP and high-pressure units were involved in top-to-NW noncoaxial shear during exhumation (Wallis et al., 1999; Faure et al., 2003; this study; Fig. 1). Petrographic observations

TABLE 3. SUMMARY OF RESULTS FOR $^{40}Ar/^{39}Ar$ ANALYSES OF K-FELDSPARS AND PARAMETERS USED IN QUALITATIVE MODELING OF THERMAL HISTORIES

Sample name	Sample locality	Apparent age (Ma)		E_a (kCal/mol)	$\log(D_0/r_0^2)$ (s^{-1})	# domains
		Minimum	Maximum			
SU01	stop 1	182.4	249.3	36.0	3.1	7
SU04	stop 1	170.8	210.2	30.0	1.6	8
SU11a	stop 9	110.3	142.2	46.0	6.0	3
SU16	stop 16	156.5	188.7	37.8	3.8	5
SU45	stop 48	102.0	201.1	35.2	3.3	6

Note: Ea—activation energy. Note that plane slab geometries yielded the best fit for all samples. For the purposes of these models, all domains were assumed to have the same activation energy.

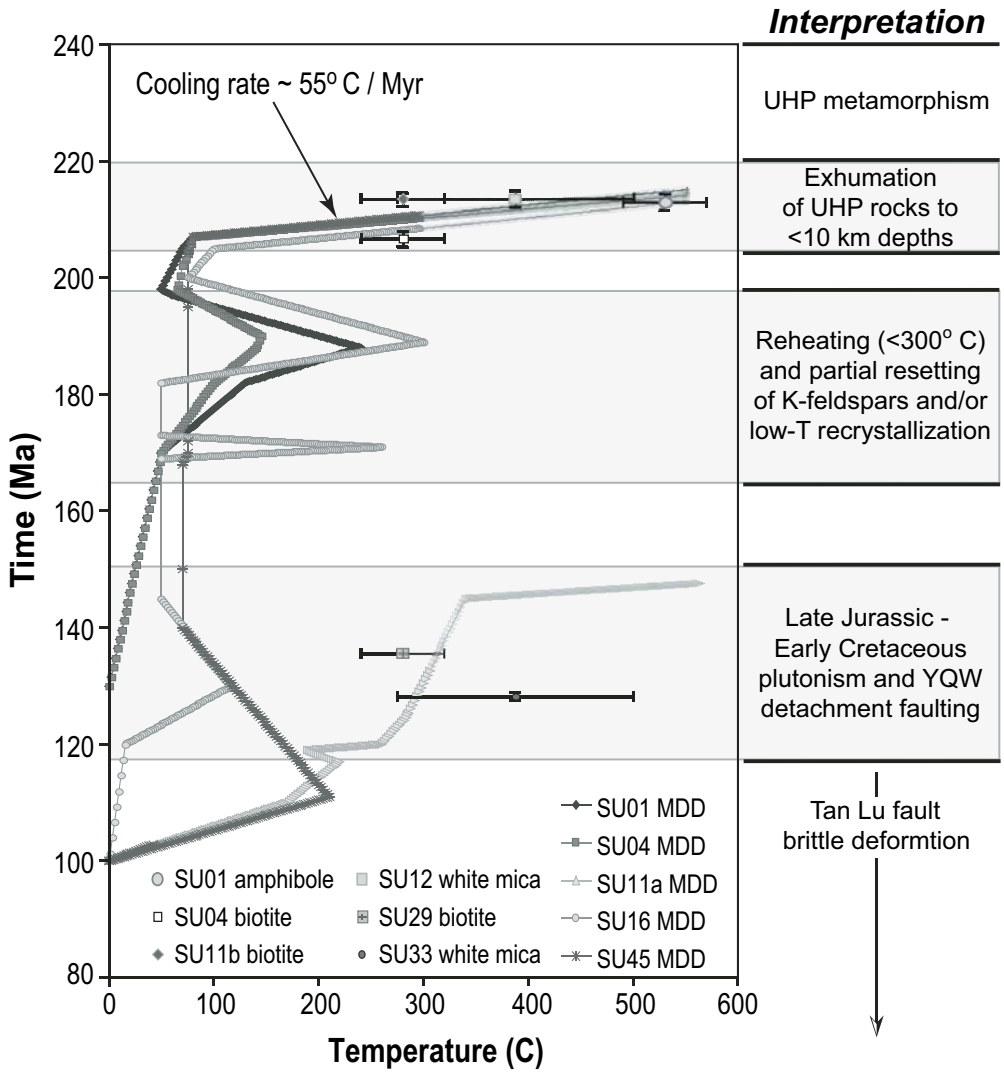

Figure 7. Temperature-time (*T-t*) plot for the Sulu terrane based on $^{40}Ar/^{39}Ar$ analyses and qualitative multi-diffusion-domain (MDD) modeling of K-feldspars. The K-feldspar thermal histories are those that yielded the best model fits to the experimental age spectra (Figs. 3 and 4). While these thermal models best constrain the *T-t* history below 300 °C, they are still sensitive to the higher-temperature history. Several samples from the high-pressure and ultrahigh-pressure (UHP) units constrain a cooling rate of 55 °C/m.y. associated with exhumation through crustal depths. Tectonic interpretations are summarized at the right and illustrate best estimates on the duration of events, as appropriate. YQW—Yantai-Qingdao-Wulian.

indicate that temperature outlasted deformation and facilitated the recovery of quartz and feldspar as the rocks cooled through biotite and K-feldspar (SU04) closure temperatures ca. 206 Ma. These data, in conjunction with thermal modeling of SU01 and SU04 K-feldspar, suggest that the UHP rocks were exhumed to upper-crustal levels by the Late Triassic ($T \approx 100$ °C; Fig. 7).

The data suggest that cooling rates of ~55 °C/m.y. accompanied exhumation through crustal depths (Fig. 7). This cooling must correspond to the portions of published *P-T* paths following near-isothermal decompression from depths associated with UHP conditions (see for example *P-T* path summaries in Wallis et al. [1999] and Faure et al. [2003]). How do the $^{40}Ar/^{39}Ar$ data bear on exhumation rates? If one assumes that the UHP rocks were at a minimum of 100 km depths at ca. 220 Ma (see Leech et al. [this volume] for a detailed discussion on the timing of UHP metamorphism and zircon growth under retrograde amphibolite-facies conditions that constrains this parameter), the Ar data suggest that by 206 Ma, the UHP rocks were at a maximum of 10 km depth. The required vertical exhumation rates are >6 mm yr^{-1}, slightly faster than those calculated by Liu et al. (2004b). Exhumation via top-to-the-NW shear along an extensional detachment fault with a dip of ≤35° requires transport along the shear zone at plate-

tectonic rates (cm yr^{-1}) through crustal depths. Such rates are in line with those that have been documented in the Hong'an portion of the orogen (Webb et al., 1999b) and are moderate in comparison to those documented in other high-pressure–UHP orogens (e.g., Rubatto and Hermann, 2001; Baldwin et al., 2004). However, a vertical exhumation rate of >6 mm yr^{-1} through the crust is fairly rapid, considering that most models for the exhumation of UHP rocks call upon buoyancy as a driving force for rapid exhumation and concede to neutral buoyancy and, thus, stagnation when the UHP rocks reach lower-crustal depths (e.g., Ernst, 2001; Walsh and Hacker, 2004).

Early and Middle Jurassic Reheating?

Evidence in this study for reheating of the Sulu high-pressure–UHP terrane in the Early Jurassic comes solely from thermal modeling of K-feldspar samples SU01, SU04, and SU16 (Fig. 7). All three models are permissive of transient reheating with temperatures peaking between ca. 190 and 187 Ma. Despite the fact that the models suggest that temperatures may have locally achieved 250–300 °C, no evidence for thermal resetting of biotite or white mica is documented in the vicinity of the respective K-feldspar sample localities. Though several spectra indicate Ar loss, it is generally of Late Jurassic–Early Cretaceous age (see low-temperature intercepts in apparent age spectra in Fig. 2). It is noteworthy, however, that there is abundant evidence in the Dabie Shan region for recrystallization of white mica (Hacker et al., 2000). White mica and biotite $^{40}Ar/^{39}Ar$ ages from that part of the orogen are commonly 195–180 Ma (Hacker and Wang, 1995; Hacker et al., 2000). In the Hong'an region, Early Jurassic $^{40}Ar/^{39}Ar$ ages ca. 195 Ma were linked to late-stage NE-SW extension under ductile-brittle conditions (Webb et al., 1999b). Whether there is any link between the modeled thermal histories for Sulu K-feldspars and the $^{40}Ar/^{39}Ar$ ages from Hong'an and Dabie is speculative. If so, the UHP rocks in Sulu reached and remained at higher structural levels in the Late Triassic–Early Jurassic compared to the Dabie Shan, where up to 15 km of Early Cretaceous exhumation has been documented (Hacker et al., 1995).

SU01 and SU04 were sampled from the UHP unit near the mapped boundary with the high-pressure unit (Fig. 1). SU16 was sampled from a chalcopyrite mine quarry in the high-pressure unit, just east of the along-strike projection of the boundary. The boundary between the high-pressure and UHP units is well defined by a regional study documenting the presence of high-pressure versus UHP mineral inclusions in zircons (Liu et al., 2004a). It has been variously mapped by some workers as the Haizhou-Siyang fault based on geophysical studies (Cong, 1996), or as a ductile shear zone based on field mapping (e.g., DF5 of Xu et al., this volume). However, structural transects conducted as part of this study yielded no evidence to support the presence of a major shear zone between the high-pressure and UHP units. If the boundary is indeed a fault, perhaps the feldspars recorded a related deformation event. However, we observed no mesoscopic or microstructural evidence to support such an interpretation. Similar thermal histories recorded by $^{40}Ar/^{39}Ar$ data from samples located on both sides of the boundary require that if the high-pressure–UHP boundary is a fault, it must have limited offset or the slip occurred before ca. 213 Ma.

The possibility of Middle Jurassic reheating is implied by the thermal model for SU16 K-feldspar (Fig. 7), as well as the younger apparent trend on the inverse isochron for sample SU04 feldspar (Fig. 6). Regional reheating, and possibly local recrystallization (e.g., SU04), may have been related to Jurassic plutonism documented in the Shandong Peninsula (e.g., Zhang et al., 2003; Xu et al., 2004). Several K-feldspar samples from the Dabie Shan modeled by Hacker et al. (2000) also suggest a thermal spike ca. 170 Ma. At present, any statement regarding the significance of this signal in the model for SU16 is premature. We note, however, that the U/Pb zircon age of ca. 166 Ma was from a granodiorite associated with a gold deposit in the northern Shandong Peninsula (Zhang et al., 2003), and sample SU16, from which the 171 Ma thermal spike was inferred, comes from a chalcopyrite mine in the high-pressure unit. One possible interpretation is that the Middle Jurassic may represent an early phase of igneous activity associated with ore genesis in the region. Plutons as old as Middle Jurassic are typically considered to be part of the Yanshanian orogeny in east China and traditionally are associated with the Pacific plate margin. However, recent geochemical and geochronological studies suggest that regional extension and igneous activity may be linked to removal of the lithospheric keel beneath the North China craton (e.g., Gao et al., 2002; Xu et al., 2004). At least some degree of Middle Jurassic regional tectonism is indicated by studies in the foreland, which reveal that siliciclastic sediments were deposited in a transpressive stress field (Grimmer et al., 2003).

Late Jurassic–Early Cretaceous Magmatism and Detachment Faulting

Early Cretaceous ages were obtained from SU11a K-feldspar, SU29 biotite, and SU30 and SU33 white mica (Fig. 2). These samples are associated with intrusive bodies and/or structures that cut the Late Triassic amphibolite-facies fabrics. The vast majority of lineations measured in the area east of the Yantai-Qingdao-Wulian fault between 35 and 36°N are oblique to lineations in the Late Triassic fabrics south of 35°N (Fig. 1). The thermochronologic data, combined with field and microstructural observations, suggest that the Yantai-Qingdao-Wulian fault was active as an Early Cretaceous top-to-the-W detachment fault. Our data are limited to the southern half of the peninsula, but studies in northern Shandong have described the Yantai-Qingdao-Wulian fault as an ~800-m-thick mylonitic-ultramylonitic shear zone (Faure et al., 2003). Wallis et al. (1999) recognized at least two stages of deformation in the vicinity of the fault, documenting E-W stretching lineations associated with top-to-the-W shear sense in a later stage of

mylonitic deformation, kinematic observations similar to ours from the Yantai-Qingdao-Wulian fault in the Wulian area, where deformation was attended by a maximum of lower greenschist-facies metamorphic conditions.

The thermochronologic data, including feldspar thermal models, suggest that extensional detachment faulting was active by 128 Ma, perhaps as early as 145 Ma, and may have continued to at least 120 Ma. In the case of SU29, from locality 37, an Early Cretaceous biotite age appears to be associated with top-to-the-S shear in dominantly L-S tectonites (Fig. 1). Feldspars and micas from the core of the orogen are largely unaffected by the Early Cretaceous extension and igneous activity, with the exception of minor Ar loss, as discussed earlier. The absence of regional resetting of the Ar systematics from samples south of 35°N suggests that Early Cretaceous exhumation in the Donghai region may have been limited to a couple of kilometers. Early Cretaceous detachment faulting along the Yantai-Qingdao-Wulian fault and plutonism on the Shandong Peninsula are temporally linked with detachment faulting and voluminous intrusions in the northern Dabie Shan (cf. Hacker et al., 1995; Ratschbacher et al., 2000). A similar time frame has been documented for Early Cretaceous extension associated with core complex formation as far inboard as southernmost Mongolia (Webb et al., 1999a). Xu et al. (2004) concluded that lithospheric thinning must have continued until the Late Cretaceous because of a change from lithospheric- to asthenospheric-sourced mafic magmas in the Shandong region west of the Yantai-Qingdao-Wulian fault at that time.

Mid to Late Cretaceous Deformation

Evidence for Late Cretaceous deformational and/or thermal resetting of Ar systematics in the Sulu terrane comes principally from samples SU17 and SU45, from localities 18 and 48, respectively (Figs. 1, 2, and 4). Sample SU17, a pseudotachylite vein that cuts the gneissic foliation, yielded an age consistent with faulting ca. 92 Ma. Sample SU45 showed evidence for late brittle deformation, and biotite yielded a complex spectrum consistent with Ar loss at ca. 70 Ma. The best-fit thermal model for SU45 K-feldspar called for reheating ca. 110 Ma, but this signal in the model could be alternatively related to deformation-related Ar loss. Though complicated, these data argue for Late Cretaceous brittle deformation in the Shandong region. We accept the possibility of a 110–75 Ma thermal pulse along the Tan-Lu fault that is indicated by K-feldspar and apatite fission-track thermochronology (Ratschbacher et al. 2000; Grimmer et al., 2002). Although the samples in our study are not from the present-day expression of the Tan-Lu fault zone, we interpret them to record deformation related to mid to Late Cretaceous sinistral-oblique slip along the Tan-Lu fault. Ratschbacher et al. (2000) documented ≥5.4 km of Cenozoic dip slip along the Tan-Lu fault, an observation that may explain why the hanging-wall Sulu terrane appears to expose shallower Mesozoic structural levels than the footwall Dabie Shan.

CONCLUSIONS

Combined structural and thermochronological studies in the Sulu terrane of eastern China document exhumation of the high-pressure and UHP metamorphic rocks from mantle to upper-crustal depths by ca. 206 Ma. Our $^{40}Ar/^{39}Ar$ dating of K-bearing phases that record recrystallization and cooling through amphibolite- and upper greenschist–facies conditions during top-to-the-NW noncoaxial shear indicates cooling rates on the order of 55 °C/m.y. Integration of the $^{40}Ar/^{39}Ar$ data with U/Pb constraints on the timing of UHP metamorphism gives vertical exhumation rates through crustal depths of >6 mm yr^{-1}. Similar thermal histories obtained from samples on both sides of the contact between the high-pressure and UHP rocks suggest that the boundary between the two units is either not a fault or was active before ca. 213 Ma.

Qualitative multi-diffusion-domain models for metamorphic feldspars sampled from the high-pressure and UHP units yield thermal histories consistent with the samples having resided at upper-crustal depths until at least Early Cretaceous time. While we cannot completely discount that samples may have experienced monotonic cooling or have been held at constant temperatures, at least three MDD models are consistent with mild to moderate reheating (<300 °C) ca. 190 Ma, followed by cooling ca. 180 Ma. One model further suggests a second thermal pulse ca. 170 Ma. Regional data from the orogen (i.e., including the Dabie Shan) are consistent with these thermal events being real. However, any thermal pulses in the Jurassic were insufficient to reset mica ages in the Sulu terrane.

The $^{40}Ar/^{39}Ar$ data also have implications for the history of Early Cretaceous extension in East Asia. The Yantai-Qingdao-Wulian fault, associated with mylonitic deformation in both the northern and southern parts of the Shandong Peninsula, was active by at least ca. 128 Ma as a top-to-the-W extensional detachment fault. Although postcollisional Mesozoic plutons are abundant on the Shandong Peninsula, they are volumetrically minor and relatively undeformed compared to the large-scale Early Cretaceous extension in the northern Dabie Shan.

The youngest phase of deformation recorded by the $^{40}Ar/^{39}Ar$ data is consistent with mid to Late Cretaceous deformation associated with sinistral-oblique slip on the Tan-Lu fault. The Tan-Lu fault, at least in its present expression, appears to truncate both the Early Cretaceous expression of the Yantai-Qingdao-Wulian fault on the Shandong Peninsula and the Xiaotian–Mozitang fault in the Dabie Shan; consideration of a possible linkage between these two detachment faults may prove useful in pre–Late Cretaceous restorations of the orogen.

Several factors suggest that the high-pressure and UHP rocks of the Sulu terrane reached and resided at higher structural levels by the Late Triassic relative to the high-pressure and UHP rocks exposed in the Dabie Shan. Significant exhumation associated with Early Cretaceous extension and later dip slip on the Tan-Lu fault has exposed rocks in the Dabie Shan that resided at deeper structural levels in Late Triassic–Early Jurassic

time. Therefore, we conclude that the $^{40}Ar/^{39}Ar$ data from the Sulu terrane presented herein provide the best constraints so far on the timing and rates of exhumation to upper-crustal depths of high-pressure and UHP rocks in the orogen.

ACKNOWLEDGMENTS

This research was supported by National Science Foundation (NSF) Continental Dynamics grant EAR-0003355 and also benefited from salary support to L.E. Webb from NSF grant EAR-IF-0130833. We would like to thank Suzanne Baldwin for discussions related to multi-diffusion-domain modeling, and reviewers B.R. Hacker, S. Johnston, J.G. Liou, M. Wong, and R.Y. Zhang for thoughtful comments that improved the manuscript.

REFERENCES CITED

Ames, L., Zhou, G., and Xiong, B., 1996, Geochronology and geochemistry of ultrahigh pressure metamorphism with implications for collision of the Sino-Korean and Yangtze cratons, central China: Tectonics, v. 15, p. 472–489, doi: 10.1029/95TC02552.

Baldwin, S.L., Monteleone, B., Webb, L.E., Fitzgerald, P.G., Grove, M., and Hill, E.J., 2004, Pliocene eclogite exhumation at plate tectonic rates in eastern Papua New Guinea: Nature, v. 431, p. 263–267, doi: 10.1038/nature02846.

Chavagnac, V., Jahn, B., Villa, I.M., Whitehouse, M.J., and Liu, D., 2001, Multichronometric evidence for an in situ origin of the ultrahigh-pressure metamorphic terrane of Dabieshan, China: The Journal of Geology, v. 109, p. 633–646, doi: 10.1086/321961.

Cong, B., 1996, Ultrahigh-pressure metamorphic rocks in the Dabieshan-Sulu region of China: Dordrecht, Netherlands, Kluwer Academic Publishers, 224 p.

Enami, M., Suzuki, K., Zhai, M., and Zheng, X., 1993, The chemical Th-U-total Pb isochron ages of Jiaodong and Jiaonan metamorphic rocks in the Shandong Peninsula, eastern China: The Island Arc, v. 2, p. 104–113.

Ernst, W.G., 2001, Subduction, ultrahigh-pressure metamorphism, and regurgitation of buoyant crustal slices—Implications for arcs and continental growth: Physics of the Earth and Planetary Interiors, v. 127, p. 253–275, doi: 10.1016/S0031-9201(01)00231-X.

Faure, M., Lin, W., and Le Breton, N., 2001, Where is the North China–South China block boundary in eastern China?: Geology, v. 29, p. 119–122, doi: 10.1130/0091-7613(2001)029<0119:WITNCS>2.0.CO;2.

Faure, M., Lin, W., Monié, P., Le Breton, N., Poussineau, S., Panis, D., and Deloule, E., 2003, Exhumation tectonics of the ultrahigh-pressure metamorphic rocks in the Qinling orogen in east China: New petrological-structural-radiometric insights from the Shandong Peninsula: Tectonics, v. 22, 1018, doi: 10.1029/2002TC001450.

Gao, S., Rudnick, R.L., Carlson, R.W., McDonough, W.F., and Liu, Y.-S., 2002, Re-Os evidence for replacement of ancient mantle lithosphere beneath the North China craton: Earth and Planetary Science Letters, v. 198, p. 307–322, doi: 10.1016/S0012-821X(02)00489-2.

Grimmer, J.C., Jonckheere, R., Enkelmann, E., Ratschbacher, L., Hacker, B.R., Blythe, A., Wagner, G.A., Liu, S. and Dong, S., 2002, Cretaceous–Tertiary history of the southern Tan-Lu fault zone: Apatite fission-track and structural constraints from the Dabie Shan: Tectonophysics, v. 359, p. 225–253.

Grimmer, J.C., Ratschbacher, L., Franz, L., Gaitzsch, I., Tichomirowa, M., McWilliams, M.O., Hacker, B.R., and Zhang, Y., 2003, When did the ultrahigh-pressure rocks reach the surface? A $^{207}Pb/^{206}Pb$ zircon, $^{40}Ar/^{39}Ar$ white mica, Si-in-phengite single grain study of Dabie Shan synorogenic foreland sediments: Chemical Geology, v. 197, p. 87–110, doi: 10.1016/S0009-2541(02)00321-2.

Hacker, B.R., and Wang, Q., 1995, Ar/Ar geochronology of ultrahigh-pressure metamorphism in central China: Tectonics, v. 14, p. 994–1006, doi: 10.1029/95TC00932.

Hacker, B.R., Ratschbacher, L., Webb, L., and Dong, S., 1995, What brought them up? Exhumation of the Dabie Shan ultrahigh-pressure rocks: Geology, v. 23, p. 743–746, doi: 10.1130/0091-7613(1995)023<0743:WBTUEO>2.3.CO;2.

Hacker, B.R., Ratschbacher, L., Webb, L., Ireland, T., Walker, D., and Dong, S., 1998, U/Pb zircon ages constrain the architecture of the ultrahigh-pressure Qinling-Dabie orogen, China: Earth and Planetary Science Letters, v. 161, p. 215–230, doi: 10.1016/S0012-821X(98)00152-6.

Hacker, B.R., Ratschbacher, L., Webb, L.E., Ireland, T.R., Calvert, A., Dong, S., Wenk, H.-R., and Chateigner, D., 2000, Exhumation of ultrahigh-pressure continental crust in east-central China: Late Triassic–Early Jurassic tectonic unroofing: Journal of Geophysical Research, v. 105, p. 13,339–13,364, doi: 10.1029/2000JB900039.

Leech, M.L., Webb, L.E., Yang, T., and Xu, Z., 2003, Microstructural analysis of the ultrahigh-pressure Sulu terrane, eastern China: Eos (Transactions, American Geophysical Union), v. 84, p. F1391.

Li, S., Ciao, Y., Liou, D., Chen, Y., Ge, N., Zhang, Z., Sun, S., Cong, B., Zhang, R., Hart, S.R., and Wang, S., 1993, Collision of the North China and Yangtse blocks and formation of coesite-bearing eclogites; timing and processes: Chemical Geology, v. 109, p. 89–111, doi: 10.1016/0009-2541(93)90063-O.

Liu, F., Xu, Z., Liou, J.G., Katayama, I., Masago, H., Maruyama, S., and Yang, J., 2002, Ultrahigh-pressure mineral inclusions in zircons from gneissic core samples of the Chinese Continental Scientific Drilling Site in eastern China: European Journal of Mineralogy, v. 14, p. 499–512.

Liu, F., Xu, Z., and Liou, J.G., 2004a, Tracing the boundary between UHP and HP metamorphic belts in the southwestern Sulu terrane, eastern China: Evidence from mineral inclusions in zircons from metamorphic rocks: International Geologic Review, v. 46, p. 409–429.

Liu, F., Xu, Z., Liou, J.G., and Song, B., 2004b, SHRIMP U-Pb ages of ultrahigh-pressure and retrograde metamorphism of gneisses, south-western Sulu terrane, eastern China: Journal of Metamorphic Geology, v. 22, p. 315–326, doi: 10.1111/j.1525-1314.2004.00516.x.

Lovera, M., Richter, F.M., and Harrison, T.M., 1989, The $^{40}Ar/^{39}Ar$ thermochronometry for slowly cooled samples having a distribution of diffusion domain sizes: Journal of Geophysical Research, v. 94, p. 17,917–17,935.

Lovera, M., Grove, M., Harrison, T.M., and Mahon, K.I., 1997, Systematic analysis of K-feldspar $^{40}Ar/^{39}Ar$ step heating results. I: Significance of activation energy determinations: Geochimica et Cosmochimica Acta, v. 61, p. 3171–3192, doi: 10.1016/S0016-7037(97)00147-6.

Lovera, M., Grove, M., and Harrison, T.M., 2002, Systematic analysis of K-feldspar $^{40}Ar/^{39}Ar$ step heating results. II: Relevance of laboratory argon diffusion properties to nature: Geochimica et Cosmochimica Acta, v. 66, p. 1237–1255, doi: 10.1016/S0016-7037(01)00846-8.

Ludwig, K.R., 2003, Isoplot/EX, rev. 3.00, A geochronological toolkit for Microsoft Excel: Berkeley Geochronology Center Special Publication, v. 4, 71 p.

McDougall, I., and Harrison, T.M., 1999, Geochronology and thermochronology by the $^{40}Ar/^{39}Ar$ method: New York, Oxford University Press, 212 p.

Parsons, I., Brown, W.L., and Smith, J.V., 1999, $^{40}Ar/^{39}Ar$ thermochronology using alkali feldspars: Real thermal history or mathematical mirage of microtexture?: Contributions to Mineralogy and Petrology, v. 136, p. 92–110, doi: 10.1007/s004100050526.

Ratschbacher, L., Hacker, B.R., Calvert, A., Webb, L.E., Ireland, T.R., McWilliams, M.O., Dong, S., Wenk, H.-R., and Chateigner, D., 2000, Exhumation of the ultrahigh-pressure continental crust in east-central China: Cretaceous and Cenozoic unroofing and the Tan-Lu fault: Journal of Geophysical Research, v. 105, p. 13,303–13,338, doi: 10.1029/2000JB900040.

Ratschbacher, L., Hacker, B.R., Calvert, A., Webb, L.E., Grimmer, J.C., McWilliams, M., Ireland, T.R., Dong, S., and Hu, J., 2003, Tectonics of the Qinling (central China): Tectonostratigraphy, geochronology, and

deformation history: Tectonophysics, v. 366, p. 1–53, doi: 10.1016/S0040-1951(03)00053-2.

Renne, P.R., Swisher, C.C., III, Deino, A.L., Karner, D.B., Owens, T., and DePaolo, D.J., 1998, Intercalibration of standards, absolute ages and uncertainties in $^{40}Ar/^{39}Ar$ dating: Chemical Geology, v. 145, p. 117–152, doi: 10.1016/S0009-2541(97)00159-9.

Rowley, D.B., Xue, F., Tucker, R.D., Peng, Z.X., Baker, J., and Davis, A., 1997, Ages of ultrahigh pressure metamorphism and protolith orthogneisses from the eastern Dabie Shan: U/Pb zircon geochronology: Earth and Planetary Science Letters, v. 151, p. 191–203, doi: 10.1016/S0012-821X(97)81848-1.

Rubatto, D., and Hermann, J., 2001, Exhumation as fast as subduction?: Geology, v. 29, p. 3–6, doi: 10.1130/0091-7613(2001)029<0003:EAFAS>2.0.CO;2.

Steiger, R.H., and Jäger, E., 1977, Subcommission on Geochronology: Convention on the use of decay constants in geo- and cosmochronology: Earth and Planetary Science Letters, v. 36, p. 359–362, doi: 10.1016/0012-821X(77)90060-7.

Wallis, S., Enami, E., and Banno, S., 1999, The Sulu UHP terrane: A review of the petrology and structural geology: International Geologic Review, v. 41, p. 906–920.

Wallis, S., Tsuboi, M., Suzuki, K., Fanning, M., Jiang, L., and Tanaka, T., 2005, Role of partial melting in the evolution of the Sulu (eastern China) ultrahigh-pressure terrane: Geology, v. 33, p. 129–132, doi: 10.1130/G20991.1.

Walsh, E.O., and Hacker, B.R., 2004, The fate of subducted continental margins: Two-stage exhumation of the high-pressure to ultrahigh-pressure Western Gneiss Region, Norway: Journal of Metamorphic Geology, v. 22, p. 671–687, doi: 10.1111/j.1525-1314.2004.00541.x.

Wartho, J.-A., 1995, Apparent argon diffusive loss $^{40}Ar/^{39}Ar$ age spectra in amphiboles: Earth and Planetary Science Letters, v. 134, p. 393–407, doi: 10.1016/0012-821X(95)00113-Q.

Webb, L.E., Graham, S.A., Johnson, C.L., Badarch, G., and Hendrix, M., 1999a, Occurrence, age, and implications of the Yagan–Onch Hayrhan metamorphic core complex, southern Mongolia: Geology, v. 27, p. 143–146, doi: 10.1130/0091-7613(1999)027<0143:OAAIOT>2.3.CO;2.

Webb, L.E., Hacker, B.R., Ratschbacher, L., McWilliams, M.O., and Dong, S., 1999b, $^{40}Ar/^{39}Ar$ thermochronologic constraints on deformation and cooling history of high and ultrahigh-pressure rocks in the Qinling-Dabie orogen: Tectonics, v. 18, p. 621–638, doi: 10.1029/1999TC900012.

Webb, L.E., Ratschbacher, L., Hacker, B.R., and Dong, S., 2001, Kinematics of exhumation of high- and ultrahigh-pressure rocks in the Hong'an and Tongbai Shan of the Qinling-Dabie collisional orogen, eastern China: Geological Society of America Memoir 194, p. 413–434.

Webb, L.E., Leech, M.L., Yang, T., and Xu, Z., 2002, Kinematics of structures of the ultrahigh-pressure Sulu terrane, eastern China: Eos (Transactions, American Geophysical Union), v. 83, p. F1245.

Xu, Y.G., Huang, X.-L., Ma, J.-L., Wang, Y.-B., Iizuka, Y., Xu, J.-F., Wang, Q., and Wu, X.-Y., 2004, Crust-mantle interaction during the tectono-thermal reactivation of the North China craton: Constraints from SHRIMP zircon U-Pb chronology and geochemistry of Mesozoic plutons from western Shandong: Contributions to Mineralogy and Petrology, v. 147, p. 750–767, doi: 10.1007/s00410-004-0594-y.

Xue, F., Rowley, D.B., Tucker, R.D., and Peng, Z.X., 1997, U-Pb zircon ages of granitoid rocks in the north Dabie complex, eastern Dabie Shan, China: The Journal of Geology, v. 105, p. 744–753.

Yang, J.S., Wooden, J.L., Wu, C.L., Liu, F.L., Xu, Z.Q., Shi, R.D., Katayama, I., Liou, J.G., and Maruyama, S., 2003, SHRIMP U-Pb dating of coesite-bearing zircon from the ultrahigh-pressure metamorphic rocks, Sulu terrane, east China: Journal of Metamorphic Geology, v. 21, p. 551–560, doi: 10.1046/j.1525-1314.2003.00463.x.

Ye, K., Liu, J., Cong, B., Ye, D., Xu, P., Omori, S., and Maruyama, S., 2002, Ultrahigh-pressure (UHP) low-Al titanites from carbonate-bearing rocks in Dabieshan-Sulu UHP terrane, eastern China: The American Mineralogist, v. 87, p. 875–881.

Yin, A., and Nie, S., 1993, An indentation model for the North and South China collision and the development of the Tanlu and Honam fault systems, eastern Asia: Tectonics, v. 12, p. 801–813.

Zhang, R.Y., and Liou, J.G., 1998, Ultrahigh-pressure metamorphism of the Sulu terrane, eastern China: A perspective view: Continental Dynamics, v. 3, p. 32–53.

Zhang, X., Cawood, P.A., Wilde, S.A., Liu, R., Song, H., Li, W., and Snee, L.W., 2003, Geology and timing of mineralization at the Cangshang gold deposit, north-western Jiaodong Peninsula, China: Mineral Deposita, v. 38, p. 141–153.

Manuscript Accepted by the Society 21 September 2005

GSA Data Repository item 2006052

From: Webb, L.E., Leech, M.L., and Yang, T.N., 2006, $^{40}Ar/^{39}Ar$ thermochronology of the Sulu terrane: Late Triassic exhumation of high- and ultrahigh-pressure rocks and implications for Mesozoic tectonics in East Asia, *in* Hacker, B.R., McClelland, W.C., and Liou, J.G., eds., Ultrahigh-pressure metamorphism: Deep continental subduction: Geological Society of America Special Paper 403, p. 77–92, doi: 10.1130/2006.2403(04).

Sample name	Phase	J factor	% error (1σ)
SU01	amphibole	1.72305E-03	0.20

Temp	Dwell Time				Cumulative			Age	2 sigma
Deg C	Minutes	37Ar/39Ar	36Ar/39Ar	39Ar (mols)	39Ar released	% 40Ar*	40Ar*/39Ar	(Ma)	error (Ma)
600	12	7.06319E-01	3.70369E+00	6.86194E-17	0.003	36.5	6.30939E+02	1327.4	52.7
650	12	8.99894E-01	8.56228E-02	1.51305E-17	0.004	80.8	1.06851E+02	304.9	20.8
700	12	9.35864E-02	6.02891E-02	2.15320E-17	0.005	83.3	8.89035E+01	257.1	15.6
775	12	1.15152E+00	7.13061E-02	7.59751E-17	0.009	77.6	7.32189E+01	214.3	7.0
850	12	1.27317E+00	1.16440E-02	1.22232E-16	0.014	95.9	8.08989E+01	235.4	3.0
900	12	1.82398E+00	3.72229E-03	6.56022E-16	0.045	98.5	7.32076E+01	214.3	1.6
940	12	2.10342E+00	2.72789E-03	1.50849E-15	0.116	98.9	7.27009E+01	212.9	1.7
970	12	2.03163E+00	1.45958E-03	1.90023E-15	0.206	99.4	7.26278E+01	212.7	1.1
1000	12	2.05641E+00	1.19108E-03	2.49965E-15	0.323	99.5	7.23974E+01	212.1	1.3
1025	12	2.07127E+00	1.92552E-03	2.80775E-15	0.455	99.2	7.25105E+01	212.4	1.0
1050	12	2.05961E+00	1.83060E-03	3.16037E-15	0.604	99.3	7.36540E+01	215.5	1.1
1075	12	2.05335E+00	1.18738E-03	2.35550E-15	0.715	99.5	7.22392E+01	211.6	1.2
1100	12	2.04458E+00	1.30619E-03	2.43929E-15	0.830	99.5	7.25279E+01	212.4	1.4
1130	12	2.06448E+00	9.73014E-04	3.31538E-15	0.986	99.6	7.22922E+01	211.8	1.2
1160	12	1.65979E+00	2.10477E-04	9.90898E-17	0.990	99.9	7.22508E+01	211.7	4.2
1220	12	1.37545E+00	5.50004E-03	1.54861E-16	0.998	97.8	7.30264E+01	213.8	4.3
1350	12	7.49557E-01	4.22838E-02	5.27026E-17	1.000	84.8	6.99983E+01	205.4	9.0

Sample name	Phase	J factor	% error (1σ)
SU04	biotite	1.72169E-03	0.11

Temp	Dwell Time				Cumulative				2 sigma
Deg C	Minutes	37Ar/39Ar	36Ar/39Ar	39Ar (mols)	39Ar released	% 40Ar*	40Ar*/39Ar	Age (Ma)	error (Ma)
600	12	1.96156E-01	1.60770E+00	9.43383E-17	0.009	9.3	4.95439E+01	147.7	33.1
650	12	3.29882E-02	7.54657E-02	7.71487E-17	0.016	75.4	6.86251E+01	201.5	7.7
690	12	7.16131E-02	1.33637E-02	1.39280E-16	0.029	94.6	6.96593E+01	204.3	2.3
730	12	4.34054E-03	2.18369E-03	3.13656E-16	0.058	99.1	6.96048E+01	204.2	1.8
765	12	2.86791E-02	1.03396E-03	6.35829E-16	0.117	99.6	7.01955E+01	205.8	1.5
800	12	6.07155E-03	5.59849E-04	1.16333E-15	0.225	99.8	7.03796E+01	206.3	0.8
830	12	7.34691E-03	6.39978E-04	8.60341E-16	0.305	99.7	7.06005E+01	207.0	0.8
860	12	1.42345E-02	1.97535E-04	5.78441E-16	0.359	99.9	7.08865E+01	207.7	1.2
900	12	9.98606E-03	7.84022E-04	6.36755E-16	0.418	99.7	7.21024E+01	211.1	1.9
940	12	6.63507E-02	2.79400E-05	8.26997E-16	0.494	100.0	7.17109E+01	210.0	3.0
980	12	2.29776E-02	8.65747E-05	1.09346E-15	0.596	100.0	7.08492E+01	207.6	1.1
1010	12	1.55407E-02	4.21627E-04	8.98285E-16	0.679	99.8	7.03807E+01	206.3	2.0
1040	12	1.29182E-02	2.93358E-04	7.63942E-16	0.750	99.9	6.99825E+01	205.2	1.5
1080	12	1.48113E-02	1.10829E-04	8.11723E-16	0.825	100.0	6.94933E+01	203.9	1.0
1120	12	1.47473E-02	1.51923E-04	8.43255E-16	0.904	99.9	7.05328E+01	206.8	2.0
1170	12	1.01047E-02	1.88994E-03	7.57353E-16	0.974	99.2	7.06103E+01	207.0	1.1
1250	12	3.07640E-02	1.65450E-02	2.79397E-16	1.000	93.4	6.94270E+01	203.7	1.6

Sample name	Phase	J factor	% error (1σ)
SU11b	biotite	1.72900E-03	0.21

Temp	Dwell Time				Cumulative				2 sigma
Deg C	Minutes	37Ar/39Ar	36Ar/39Ar	39Ar (mols)	39Ar released	% 40Ar*	40Ar*/39Ar	Age (Ma)	error (Ma)
550	12	5.92483E-02	1.15287E+00	2.26672E-16	0.011	12.8	5.04047E+01	150.7	12.3
600	12	4.61942E-03	1.46712E-02	4.55708E-16	0.033	94.1	6.92385E+01	204.0	1.5
650	12	2.42607E-02	3.31382E-03	9.11194E-16	0.077	98.7	7.36732E+01	216.3	1.5
690	12	2.28312E-03	1.27440E-03	1.20556E-15	0.134	99.5	7.30407E+01	214.6	1.3
730	12	8.64350E-04	1.32121E-03	1.80810E-15	0.221	99.5	7.27637E+01	213.8	1.0
760	12	2.76153E-03	7.24543E-04	1.61914E-15	0.299	99.7	7.23579E+01	212.7	1.0
790	12	6.76776E-03	5.51986E-04	1.07978E-15	0.351	99.8	7.26025E+01	213.3	1.1
820	12	5.51748E-03	8.15841E-04	6.04916E-16	0.380	99.7	7.36848E+01	216.3	1.8
860	12	1.26231E-02	1.29183E-03	5.52504E-16	0.407	99.5	7.23850E+01	212.7	2.1
910	12	2.18433E-02	1.14474E-03	7.78610E-16	0.444	99.5	7.26787E+01	213.6	1.5
955	12	6.75804E-02	2.62191E-04	1.35514E-15	0.509	99.9	7.32934E+01	215.3	0.8
1000	12	1.00330E-02	3.22152E-04	2.34606E-15	0.622	99.9	7.23301E+01	212.6	0.9
1050	12	1.02765E-02	3.73273E-04	2.75681E-15	0.754	99.8	7.19538E+01	211.5	0.9
1100	12	1.69490E-02	4.78160E-04	2.69971E-15	0.884	99.8	7.20576E+01	211.8	1.1
1150	12	9.13008E-02	4.23398E-04	1.89876E-15	0.975	99.8	7.24476E+01	212.9	0.9
1200	12	2.97766E-01	1.51237E-03	4.06434E-16	0.995	99.4	7.28330E+01	214.0	2.1
1350	12	3.02773E-01	2.34892E-06	1.13281E-16	1.000	100.0	7.23415E+01	212.6	2.2

Sample name	Phase	J factor	% error (1σ)
SU12	white mica	1.73278E-03	0.21

Temp	Dwell Time				Cumulative				2 sigma
Deg C	Minutes	37Ar/39Ar	36Ar/39Ar	39Ar (mols)	39Ar released	% 40Ar*	40Ar*/39Ar	Age (Ma)	error (Ma)
600	12	2.02890E-01	7.28014E+00	9.63741E-17	0.006	1.6	3.82623E+01	115.8	100.5
650	12	1.09207E-01	7.92204E-02	6.45570E-17	0.009	75.4	7.19316E+01	211.9	2.6
700	12	2.50384E-02	4.71272E-03	1.07136E-16	0.016	98.2	7.51308E+01	220.8	2.6
750	12	1.01765E-02	1.52978E-02	1.93297E-16	0.027	94.2	7.40395E+01	217.8	3.5
790	12	1.94725E-02	2.05015E-02	3.17998E-16	0.045	92.4	7.33943E+01	216.0	2.1
820	12	7.59708E-03	1.48417E-02	1.15991E-15	0.112	94.3	7.25680E+01	213.7	1.4
850	12	7.74508E-04	4.26235E-03	2.95739E-15	0.283	98.3	7.17648E+01	211.5	1.3
870	12	2.81215E-03	1.05226E-03	2.67505E-15	0.438	99.6	7.21708E+01	212.6	1.1
890	12	4.71793E-03	9.01241E-04	2.01964E-15	0.555	99.6	7.25533E+01	213.6	1.2
920	12	2.53968E-03	1.33833E-03	1.63843E-15	0.650	99.5	7.24442E+01	213.3	1.2
960	12	1.46264E-04	2.69047E-03	1.23566E-15	0.722	98.9	7.28369E+01	214.4	1.3
1020	12	2.34792E-03	1.90893E-03	1.57699E-15	0.813	99.2	7.21628E+01	212.6	1.2
1100	12	4.07606E-03	6.64686E-04	2.75480E-15	0.972	99.7	7.20954E+01	212.4	1.2
1180	12	9.51465E-02	5.21737E-04	3.17074E-16	0.991	99.8	7.40920E+01	217.9	1.6
1350	12	1.99648E-01	5.85290E-03	1.62011E-16	1.000	97.7	7.35889E+01	216.5	1.5

Sample name	Phase	J factor	% error (1σ)
SU17	pseudotachylyte	1.73474E-03	0.05

Temp	Dwell Time				Cumulative				2 sigma
Deg C	Minutes	37Ar/39Ar	36Ar/39Ar	39Ar (mols)	39Ar released	% 40Ar*	40Ar*/39Ar	Age (Ma)	error (Ma)
550	12	4.21921E-02	1.04897E-01	9.96514E-16	0.082	50.6	3.18060E+01	96.9	1.3
600	12	1.17094E-01	2.98312E-03	8.77854E-16	0.154	97.0	2.88793E+01	88.2	0.7
650	12	2.65082E-01	1.14646E-03	1.15679E-15	0.249	98.8	2.84543E+01	86.9	0.6
700	12	4.32698E-01	4.55440E-04	1.35218E-15	0.360	99.5	2.91950E+01	89.1	0.6
750	12	4.86182E-01	3.63723E-04	1.34194E-15	0.470	99.6	3.01845E+01	92.1	0.5
800	12	1.02604E-01	2.67090E-04	1.09433E-15	0.560	99.7	3.03066E+01	92.4	0.7
850	12	2.46747E-02	3.58565E-04	8.89971E-16	0.633	99.7	3.02195E+01	92.2	0.5
910	12	4.06232E-02	5.23852E-04	7.99763E-16	0.699	99.5	3.01247E+01	91.9	0.6
975	12	8.73329E-02	3.81387E-04	7.67537E-16	0.762	99.6	3.08863E+01	94.2	0.7
1050	12	1.02174E-01	1.16138E-03	8.51269E-16	0.832	98.9	3.19781E+01	97.4	0.5
1125	12	1.74067E-02	5.05142E-03	9.41410E-16	0.910	96.8	4.50152E+01	135.6	0.7
1200	12	1.01439E-01	1.77883E-03	5.13866E-16	0.952	98.6	3.73038E+01	113.1	0.8
1350	12	3.87555E-01	2.18702E-03	3.59490E-16	0.981	98.6	4.62552E+01	139.2	1.4
1500	12	3.15998E-01	1.56994E-02	2.27998E-16	1.000	92.2	5.51467E+01	164.8	1.5

Sample name	Phase	J factor	% error (1σ)
SU29	biotite	1.73066E-03	0.05

Temp	Dwell Time				Cumulative				2 sigma
Deg C	Minutes	37Ar/39Ar	36Ar/39Ar	39Ar (mols)	39Ar released	% 40Ar*	40Ar*/39Ar	Age (Ma)	error (Ma)
550	12	1.17026E-01	2.97030E+00	1.40621E-16	0.012	4.8	4.52485E+01	136.0	27.5
600	12	3.77749E-02	3.17643E-02	1.68903E-16	0.027	82.4	4.40709E+01	132.6	1.7
650	12	2.54107E-02	1.43537E-02	3.75478E-16	0.059	91.4	4.50768E+01	135.5	1.3
700	12	1.29285E-02	3.92895E-03	7.54546E-16	0.123	97.5	4.54168E+01	136.5	0.7
740	12	9.84682E-03	1.86980E-03	1.00864E-15	0.210	98.8	4.48792E+01	134.9	0.6
775	12	9.29119E-03	1.35504E-03	9.61107E-16	0.292	99.1	4.48972E+01	135.0	0.6
810	12	1.02703E-02	1.64197E-03	6.97710E-16	0.352	98.9	4.52652E+01	136.1	1.5
850	12	9.49418E-03	2.82640E-03	5.45707E-16	0.399	98.2	4.51252E+01	135.7	1.2
900	12	1.40672E-02	4.32623E-03	5.64565E-16	0.447	97.2	4.47626E+01	134.6	1.5
940	12	1.87979E-02	5.95311E-03	5.49339E-16	0.494	96.3	4.55590E+01	136.9	1.0
975	12	1.22742E-02	4.99856E-03	9.41335E-16	0.575	96.8	4.49968E+01	135.3	0.7
1010	12	1.18202E-02	3.20035E-03	1.15841E-15	0.674	97.9	4.50521E+01	135.4	0.8
1050	12	4.47438E-03	2.62906E-03	1.22895E-15	0.780	98.3	4.48945E+01	135.0	0.7
1100	12	3.70092E-02	2.28516E-03	1.47637E-15	0.906	98.5	4.54453E+01	136.6	0.7
1175	12	1.70368E-01	1.44688E-03	1.00084E-15	0.992	99.1	4.77615E+01	143.3	0.6
1350	12	1.00086E+00	1.77062E-02	9.21839E-17	1.000	90.4	4.96401E+01	148.7	2.6

Sample name	Phase	J factor	% error (1σ)
SU30	white mica	1.72575E-03	0.05

Temp	Dwell Time				Cumulative				2 sigma
Deg C	Minutes	37Ar/39Ar	36Ar/39Ar	39Ar (mols)	39Ar released	% 40Ar*	40Ar*/39Ar	Age (Ma)	error (Ma)
600	12	3.92370E-02	4.53245E-01	2.91251E-16	0.027	26.7	4.89042E+01	146.2	6.6
650	12	8.25148E-03	3.79334E-02	2.10715E-16	0.047	80.7	4.70456E+01	140.8	2.0
700	12	5.69590E-04	6.00184E-03	1.22230E-15	0.161	96.8	5.37212E+01	159.9	1.7
730	12	6.13849E-03	2.44382E-03	1.07023E-15	0.262	98.7	5.31840E+01	158.4	0.6
760	12	1.70958E-02	2.12423E-03	1.00595E-15	0.356	98.8	5.28500E+01	157.5	1.5
790	12	4.47256E-03	1.05084E-03	1.79314E-15	0.524	99.4	5.28368E+01	157.4	0.8
815	12	3.41558E-03	7.04218E-04	8.49727E-16	0.603	99.6	5.27878E+01	157.3	1.6
840	12	3.93402E-03	1.13134E-03	9.73915E-16	0.694	99.4	5.24782E+01	156.4	1.5
870	12	2.07550E-03	6.36758E-04	1.01209E-15	0.789	99.6	5.32939E+01	158.7	0.9
900	12	4.06327E-03	4.75817E-04	8.65912E-16	0.870	99.7	5.31324E+01	158.3	1.1
940	12	4.44519E-03	4.53850E-04	8.69750E-16	0.952	99.7	5.27214E+01	157.1	0.8
980	12	1.00949E-01	3.97838E-03	1.47672E-16	0.965	97.7	5.02065E+01	149.9	2.5
1050	12	8.47449E-02	1.99737E-03	8.59483E-17	0.973	98.9	5.10080E+01	152.2	2.9
1175	12	1.36528E-01	4.10659E-03	8.58625E-17	0.981	97.5	4.74873E+01	142.1	2.8
1350	12	4.56453E-02	8.53910E-04	1.98394E-16	1.000	99.5	5.51895E+01	164.1	4.1

Sample name	Phase	J factor	% error (1σ)
SU33	white mica	1.72083E-03	0.21

Temp	Dwell Time				Cumulative				2 sigma
Deg C	Minutes	37Ar/39Ar	36Ar/39Ar	39Ar (mols)	39Ar released	% 40Ar*	40Ar*/39Ar	Age (Ma)	error (Ma)
600	12	1.12154E-01	2.50491E+00	8.52203E-17	0.004	5.5	4.42341E+01	132.3	24.9
650	12	1.81953E-02	4.33301E-01	8.21523E-17	0.009	25.1	4.30698E+01	129.0	2.9
700	12	5.02929E-02	1.66134E-01	1.42844E-16	0.016	47.7	4.48943E+01	134.3	3.4
750	12	1.48303E-02	6.24769E-02	3.13773E-16	0.032	70.3	4.36823E+01	130.8	1.3
800	12	4.20166E-03	1.31817E-02	1.55264E-15	0.113	91.8	4.34340E+01	130.0	0.9
840	12	2.05916E-04	2.15483E-03	4.08022E-15	0.325	98.5	4.27737E+01	128.1	0.7
870	12	3.29712E-03	9.42793E-04	3.77357E-15	0.522	99.4	4.26444E+01	127.8	0.7
900	12	1.22350E-03	1.10850E-03	2.40602E-15	0.647	99.2	4.28695E+01	128.4	0.8
940	12	3.55408E-03	2.01304E-03	1.72046E-15	0.736	98.6	4.29473E+01	128.6	0.6
990	12	3.03865E-05	2.25133E-03	1.45723E-15	0.812	98.5	4.26395E+01	127.7	0.8
1050	12	2.92633E-03	4.81277E-04	2.38296E-15	0.936	99.7	4.27525E+01	128.1	0.7
1100	12	7.09127E-04	3.20091E-05	1.03150E-15	0.989	100.0	4.31066E+01	129.1	1.0
1200	12	6.92457E-02	2.37672E-03	2.02282E-16	1.000	98.4	4.32916E+01	129.6	1.2

Sample name	Phase	J factor	% error (1σ)
SU45	biotite	1.72332E-03	0.07

Temp	Dwell Time				Cumulative				2 sigma
Deg C	Minutes	37Ar/39Ar	36Ar/39Ar	39Ar (mols)	39Ar released	% 40Ar*	40Ar*/39Ar	Age (Ma)	error (Ma)
550	12	8.19619E+00	4.11693E-01	6.48281E-16	0.287	9.2	1.35033E+01	41.5	2.1
620	12	1.01704E+01	5.77541E-02	3.33779E-16	0.434	55.0	2.19363E+01	66.9	1.0
650	12	2.08461E+00	5.25968E-02	3.90851E-16	0.607	59.3	2.29384E+01	69.9	0.6
740	12	7.96573E+00	5.24531E-02	3.42179E-16	0.758	59.0	2.31338E+01	70.5	1.4
790	12	1.28533E+01	5.14443E-02	2.22607E-16	0.856	59.1	2.32785E+01	71.0	1.0
840	12	6.48845E+01	5.16987E-02	7.92613E-17	0.892	59.1	2.85779E+01	86.7	2.1
900	12	2.21514E+01	5.27703E-02	5.38763E-17	0.915	62.2	2.79488E+01	84.9	2.6
975	12	5.69667E+01	4.45624E-02	9.02100E-17	0.955	63.8	2.89115E+01	87.7	1.4
1075	12	1.83410E+01	4.03052E-02	9.07133E-17	0.995	67.4	2.65277E+01	80.6	1.3
1200	12	2.87058E+02	3.58295E-02	1.06125E-17	1.000	78.2	7.59523E+01	221.9	7.5

Sample name	Phase	J factor	% error (1σ)
SU01	K-feldspar	1.72227E-03	0.20

Temp	Dwell Time				Cumulative				2 sigma
Deg C	Minutes	37Ar/39Ar	36Ar/39Ar	39Ar (mols)	39Ar released	% 40Ar*	40Ar*/39Ar	Age (Ma)	error (Ma)
450	12	4.20185E-01	4.51514E+00	5.90843E-17	0.004	51.3	1.41179E+03	2224.4	20.7
480	12	1.24247E+00	4.24852E-01	4.59331E-17	0.007	52.7	1.40459E+02	390.9	5.6
500	12	5.61777E-01	3.49896E-02	5.36722E-17	0.010	88.7	8.10103E+01	235.6	2.5
530	12	6.21362E-01	8.07648E-02	9.54050E-17	0.017	83.3	1.19012E+02	336.4	3.4
560	12	3.60926E-01	4.95566E-02	1.42890E-16	0.026	87.5	1.02378E+02	293.0	2.8
590	12	2.68553E-01	7.30584E-02	2.36864E-16	0.041	85.1	1.23359E+02	347.6	3.4
620	12	2.88660E-01	1.91943E-02	1.76157E-16	0.053	92.7	7.24117E+01	212.0	2.0
620	25	5.59441E-01	1.09727E-02	1.47858E-16	0.063	95.0	6.17790E+01	182.4	1.8
650	12	4.83635E-01	1.70068E-04	1.16248E-16	0.070	99.9	6.38825E+01	188.3	1.7
680	12	5.06519E-01	8.73967E-03	1.85059E-16	0.082	96.3	6.78407E+01	199.4	1.9
710	12	2.15074E-01	2.87110E-02	2.51392E-16	0.099	89.8	7.50455E+01	219.3	2.2
740	12	2.52588E-01	1.77094E-04	2.62428E-16	0.116	99.9	6.42316E+01	189.3	1.7
740	25	1.75374E-01	3.33428E-04	2.68161E-16	0.133	99.8	6.21292E+01	183.4	1.6
770	12	2.94628E-01	1.88022E-02	1.90236E-16	0.146	92.2	6.57086E+01	193.4	3.6
800	12	3.66286E-01	6.53405E-03	2.42584E-16	0.162	97.1	6.44236E+01	189.8	1.7
835	12	1.40255E-01	4.58750E-03	3.01604E-16	0.181	97.9	6.44172E+01	189.8	1.7
870	12	3.31428E-01	1.43586E-03	3.28054E-16	0.203	99.3	6.31366E+01	186.2	1.6
870	25	1.52297E-01	6.10113E-03	3.07818E-16	0.223	97.2	6.31658E+01	186.3	1.7
900	12	5.50580E-01	7.90197E-03	1.77567E-16	0.235	96.4	6.29701E+01	185.8	1.7
935	12	3.31341E-01	5.38640E-03	2.38833E-16	0.250	97.6	6.44087E+01	189.8	1.7
970	12	2.16959E-01	3.95194E-03	2.74082E-16	0.268	98.2	6.35738E+01	187.4	1.7
1000	25	4.17471E-04	8.67174E-04	2.94688E-16	0.287	99.6	6.45444E+01	190.2	1.7
1000	12	8.72286E-02	4.19471E-03	2.65315E-16	0.305	98.1	6.47815E+01	190.8	1.7
1030	12	9.51183E-02	1.39239E-03	1.73713E-16	0.316	99.4	6.88437E+01	202.1	1.7
1060	12	2.15665E-02	6.68979E-03	2.24400E-16	0.331	97.3	7.05290E+01	206.8	1.9
1080	12	5.41989E-02	1.30008E-02	2.34065E-16	0.346	94.9	7.23245E+01	211.8	2.0
1100	12	7.33522E-02	1.86692E-02	2.80599E-16	0.364	93.1	7.42519E+01	217.1	2.0
1100	25	8.61546E-02	1.98161E-02	3.96385E-16	0.390	92.8	7.60066E+01	221.9	2.1
1100	50	9.33752E-02	2.02511E-02	5.21980E-16	0.424	93.0	7.91319E+01	230.5	2.1
1150	12	8.81091E-02	3.22056E-02	4.22100E-16	0.452	89.3	7.99765E+01	232.8	2.2
1200	12	2.44306E-02	3.09000E-02	1.39447E-15	0.543	89.7	7.97434E+01	232.2	2.1
1250	12	4.56617E-01	2.26986E-02	3.03062E-15	0.741	92.7	8.60490E+01	249.3	2.2
1300	12	6.09721E-03	2.41239E-02	1.85247E-15	0.862	92.3	8.53681E+01	247.5	2.2
1350	12	3.88061E-02	3.59846E-02	3.53511E-16	0.885	88.8	8.48825E+01	246.2	2.3
1400	12	2.93641E-02	2.99005E-02	9.32855E-16	0.946	90.4	8.30586E+01	241.2	2.2
1450	12	2.64068E-02	1.44148E-02	7.77709E-16	0.997	95.1	8.35285E+01	242.5	2.1
1500	12	2.71316E+00	4.21289E-01	4.12541E-17	1.000	39.5	8.19596E+01	238.2	4.7

Sample name	Phase	J factor	% error (1σ)
SU04	K-feldspar	1.72645E-03	0.07

Temp	Dwell Time				Cumulative				2 sigma
Deg C	Minutes	37Ar/39Ar	36Ar/39Ar	39Ar (mols)	39Ar released	% 40Ar*	40Ar*/39Ar	Age (Ma)	error (Ma)
450	12	9.90452E-01	6.81119E+00	7.29996E-17	0.006	17.1	4.22400E+02	988.1	35.1
500	12	9.59857E-01	5.81350E-02	7.53553E-17	0.013	77.6	5.98267E+01	177.3	1.8
550	12	7.55796E-01	3.28699E-02	1.47335E-16	0.026	87.0	6.53735E+01	192.9	1.8
600	12	3.76828E-01	1.41933E-02	1.51759E-16	0.039	94.1	6.65312E+01	196.2	1.6
600	25	4.08451E-02	1.74306E-03	9.39626E-17	0.047	99.1	5.75116E+01	170.8	1.4
650	12	7.43359E-01	2.73063E-02	1.19737E-16	0.057	89.6	6.97464E+01	205.1	1.9
700	12	3.56759E-01	7.79810E-03	2.06764E-16	0.075	96.5	6.45137E+01	190.5	1.6
750	12	7.95725E-02	4.27077E-03	2.85966E-16	0.100	98.0	6.13316E+01	181.6	1.5
800	12	1.20901E-02	5.71197E-03	3.22050E-16	0.127	97.4	6.30504E+01	186.4	1.6
840	12	1.39861E-01	5.07763E-03	2.68752E-16	0.151	97.7	6.27498E+01	185.6	1.6
840	38	3.40762E-02	1.86129E-03	2.87194E-16	0.175	99.1	6.19250E+01	183.2	1.5
880	12	2.11501E-02	5.39467E-03	1.26596E-16	0.186	97.5	6.26672E+01	185.3	1.6
920	12	3.70226E-01	2.99174E-03	2.12060E-16	0.202	98.6	6.08425E+01	180.2	1.4
960	12	1.87933E-02	7.05912E-03	2.12060E-16	0.221	96.8	6.32831E+01	187.1	1.5
1000	12	1.61639E-01	7.72203E-03	2.41100E-16	0.241	96.5	6.35572E+01	187.8	1.5
1035	25	1.76672E-01	1.11948E-02	4.92844E-16	0.284	95.2	6.59179E+01	194.4	1.6
1035	50	1.06128E-01	2.15500E-03	5.65389E-16	0.333	99.1	6.84404E+01	201.5	1.6
1070	25	4.65974E-02	8.59912E-03	4.89264E-16	0.375	96.5	6.93192E+01	203.9	1.6
1100	25	1.64511E-01	1.45873E-02	7.02159E-16	0.436	94.2	7.01696E+01	206.3	1.7
1100	50	1.62487E-01	1.57429E-03	6.54184E-16	0.492	99.3	7.00174E+01	205.9	1.6
1100	75	2.26576E-01	3.62027E-03	4.40855E-16	0.530	98.5	6.93354E+01	204.0	1.6
1150	12	3.72625E-01	4.18616E-03	2.90126E-16	0.555	98.3	7.05099E+01	207.2	1.6
1200	12	9.57320E-02	8.65050E-03	9.57117E-16	0.638	96.5	7.05227E+01	207.3	1.3
1250	12	1.93259E+01	8.40144E-03	1.61569E-15	0.778	96.5	7.15624E+01	210.2	1.6
1300	12	1.56972E-02	7.06400E-03	1.29642E-15	0.890	97.1	6.97222E+01	205.1	1.6
1350	12	1.85134E-01	7.30235E-03	5.63510E-16	0.938	97.0	7.01773E+01	206.3	1.6
1400	12	9.52830E-01	1.08295E-02	1.84811E-16	0.954	95.6	6.93379E+01	204.0	1.7
1500	12	1.09593E-01	3.49785E-02	5.30420E-16	1.000	87.2	7.02971E+01	206.7	1.8

Sample name	Phase	J factor	% error (1σ)
SU11a	K-feldspar	1.72417E-03	0.10

Temp	Dwell Time				Cumulative				2 sigma
Deg C	Minutes	37Ar/39Ar	36Ar/39Ar	39Ar (mols)	39Ar released	% 40Ar*	40Ar*/39Ar	Age (Ma)	error (Ma)
450	12	3.00422E+00	2.74419E+00	5.10154E-17	0.003	7.3	6.60977E+01	194.7	45.9
490	12	1.10629E+00	1.40090E-01	7.18023E-17	0.008	46.7	3.65599E+01	110.3	2.8
530	12	7.82662E-01	2.36078E-02	1.57508E-16	0.018	84.1	3.69650E+01	111.5	1.9
570	12	7.18557E-01	1.21784E-02	1.81030E-16	0.029	91.2	3.72422E+01	112.3	0.6
570	25	9.47431E-01	5.35042E-03	1.33838E-16	0.038	96.0	3.82767E+01	115.3	1.7
610	14	6.06528E-01	6.65918E-03	1.56574E-16	0.048	95.2	3.92214E+01	118.1	1.9
650	25	4.72772E-01	1.69558E-02	2.65157E-16	0.065	88.8	3.98697E+01	119.9	0.9
690	12	6.36173E-01	4.87097E-03	1.50917E-16	0.074	96.4	3.86210E+01	116.3	1.4
690	25	1.21610E+00	2.76214E-03	1.20220E-16	0.082	98.0	3.92509E+01	118.1	1.9
730	12	4.89309E-01	1.53287E-02	8.34075E-17	0.087	89.6	3.89817E+01	117.4	2.9
770	12	6.61655E-01	1.00844E-01	1.51193E-16	0.097	59.6	4.42069E+01	132.5	2.1
800	12	1.46746E+00	3.43656E-02	8.78558E-17	0.102	79.2	3.88698E+01	117.0	1.3
800	50	6.96284E-01	1.20645E-02	5.85054E-17	0.111	91.5	3.85033E+01	116.0	1.4
835	12	2.44489E+00	4.45356E-02	5.85054E-17	0.115	75.0	3.97908E+01	119.7	2.7
870	12	4.17255E-02	6.62566E-02	1.04222E-16	0.121	66.4	3.87334E+01	116.6	1.9
900	12	3.17778E-01	5.06759E-02	1.65468E-16	0.132	73.1	4.09106E+01	123.0	1.7
925	25	1.59024E-01	4.83485E-02	4.00045E-16	0.157	74.4	4.16821E+01	125.2	1.7
950	25	1.89396E-01	5.18467E-02	6.39820E-16	0.198	72.9	4.14421E+01	124.5	0.8
975	25	1.02006E-01	4.75643E-02	9.06723E-16	0.255	74.6	4.14485E+01	124.5	1.3
1000	25	1.68693E-02	4.28359E-02	1.15031E-15	0.328	76.7	4.17743E+01	125.5	0.7
1025	25	1.38862E-02	3.71331E-02	1.32704E-15	0.412	79.2	4.19660E+01	126.0	0.8
1050	25	2.14584E-02	3.11201E-02	1.55998E-15	0.511	82.2	4.24873E+01	127.5	0.7
1075	25	1.18879E-01	2.43248E-02	1.69647E-15	0.619	85.8	4.35797E+01	130.7	0.7
1100	25	1.96855E-02	1.78012E-02	1.87696E-15	0.738	89.4	4.42383E+01	132.6	0.8
1100	50	3.22583E-03	1.87653E-02	1.08409E-15	0.807	88.8	4.41386E+01	132.3	0.7
1100	75	1.02750E-02	1.34947E-02	2.20496E-15	0.947	92.0	4.61467E+01	138.1	0.7
1150	12	2.47661E-01	5.40325E-03	1.28812E-16	0.955	96.6	4.56008E+01	136.5	2.2
1200	12	2.22363E-01	1.48512E-02	2.12204E-16	0.968	91.5	4.75713E+01	142.2	1.0
1250	12	4.91698E-01	4.85552E-02	1.03529E-16	0.975	76.0	4.57301E+01	136.9	2.2
1350	12	3.56062E-01	7.12635E-02	9.32260E-17	0.981	68.6	4.61511E+01	138.1	2.3
1500	12	4.00487E-01	3.26963E-02	3.01264E-16	1.000	82.1	4.44334E+01	133.2	2.1

Sample name	Phase	J factor	% error (1σ)
SU16	K-feldspar	1.74047E-03	0.21

Temp	Dwell Time				Cumulative				2 sigma
Deg C	Minutes	37Ar/39Ar	36Ar/39Ar	39Ar (mols)	39Ar released	% 40Ar*	40Ar*/39Ar	Age (Ma)	error (Ma)
450	12	9.99855E-01	1.27873E+00	7.37124E-17	0.005	37.0	2.23957E+02	593.8	13.4
500	12	6.05931E-01	4.36843E-02	1.14469E-16	0.012	80.1	5.20787E+01	156.5	2.0
550	12	3.66974E-01	1.04259E-02	2.25114E-16	0.027	94.5	5.25726E+01	158.0	1.8
600	12	2.28322E-01	7.87518E-03	4.01556E-16	0.053	96.0	5.60402E+01	167.9	1.5
640	12	3.33147E-01	4.59529E-03	3.57304E-16	0.077	97.7	5.74973E+01	172.1	1.7
680	12	2.38210E-01	3.12701E-03	3.12027E-16	0.097	98.4	5.81071E+01	173.8	1.6
680	25	1.70215E-01	3.90649E-03	4.36017E-16	0.126	98.1	5.82592E+01	174.2	1.1
720	12	9.11670E-01	6.31250E-03	1.97595E-16	0.139	96.9	5.75033E+01	172.1	1.5
760	12	1.81654E-01	2.26135E-03	2.23857E-16	0.153	98.8	5.71833E+01	171.2	1.4
800	12	7.10814E-01	4.17707E-03	2.71386E-16	0.171	97.9	5.77842E+01	172.9	2.1
840	12	2.45955E-01	8.33333E-03	2.79292E-16	0.189	95.9	5.78834E+01	173.2	1.4
840	25	1.92911E-01	8.05924E-03	2.43353E-16	0.205	96.0	5.72124E+01	171.3	2.2
880	12	4.74524E-01	5.03285E-03	2.31129E-16	0.216	97.5	5.75998E+01	172.4	2.3
920	12	4.32336E-01	1.01683E-02	2.31129E-16	0.231	95.0	5.75548E+01	172.2	2.2
960	12	3.90648E-01	6.70884E-03	2.74576E-16	0.249	96.6	5.71957E+01	171.2	1.6
1000	25	1.26146E-01	6.38822E-03	4.86417E-16	0.281	96.8	5.73530E+01	171.7	1.1
1035	25	1.95514E-01	1.38903E-02	4.75545E-16	0.312	93.4	5.85230E+01	175.0	1.2
1035	50	2.10149E-01	5.07671E-04	5.32752E-16	0.347	99.8	5.95487E+01	177.9	1.2
1070	25	2.66507E-01	2.12953E-02	3.76403E-16	0.371	90.5	6.02212E+01	179.8	2.2
1100	25	1.54468E-01	1.14870E-02	5.61811E-16	0.408	94.7	6.02580E+01	179.9	1.6
1100	50	3.06920E-01	2.72073E-03	2.21147E-16	0.423	98.7	6.02931E+01	180.0	2.9
1100	75	7.96463E-01	2.06260E-02	1.96954E-16	0.436	90.9	6.11696E+01	182.5	2.6
1175	12	1.92952E-01	1.20927E-02	3.07578E-16	0.456	94.5	6.17689E+01	184.2	1.7
1250	12	1.21392E-02	1.65229E-02	1.07543E-15	0.526	92.6	6.13608E+01	183.1	1.2
1350	12	4.85527E-01	1.56337E-02	3.90725E-15	0.781	93.2	6.30517E+01	187.9	1.6
1500	12	1.67796E-02	8.40117E-03	3.33846E-15	1.000	96.2	6.33622E+01	188.7	1.2
1600	12	1.19070E+01	1.73856E+01	4.23798E-18	1.000	0.9	6.27078E+01	186.9	1066.1

Sample name	Phase	J factor	% error (1σ)
SU45	K-feldspar	1.72527E-03	0.07

Temp	Dwell Time				Cumulative				2 sigma
Deg C	Minutes	37Ar/39Ar	36Ar/39Ar	39Ar (mols)	39Ar released	% 40Ar*	40Ar*/39Ar	Age (Ma)	error (Ma)
450	12	2.19957E+00	9.64609E+00	3.93404E-17	0.004	20.7	7.52099E+02	1500.7	90.3
490	12	4.72307E-01	1.10676E+00	7.90599E-17	0.013	32.1	1.55515E+02	428.8	31.0
530	12	5.03008E-01	3.46470E-02	1.49067E-16	0.028	89.9	9.16291E+01	264.8	2.5
560	12	3.17196E-01	1.01928E-02	1.53360E-16	0.045	95.0	5.78401E+01	171.6	2.6
560	25	3.02381E-01	3.88943E-03	1.23763E-16	0.058	97.7	4.85109E+01	145.0	1.4
590	12	3.02381E-01	1.52808E-02	1.23763E-16	0.071	91.5	4.88265E+01	145.9	1.5
620	12	1.18267E-01	2.37569E-02	1.76159E-16	0.090	91.1	7.18362E+01	210.8	2.4
650	12	2.99141E-01	3.99675E-03	1.70721E-16	0.108	96.8	3.60943E+01	109.0	1.3
650	25	1.21456E-01	3.10071E-03	2.05657E-16	0.130	97.4	3.46124E+01	104.6	1.1
680	12	3.72683E-01	1.30828E-02	1.85058E-16	0.150	94.6	6.72965E+01	198.2	1.5
710	12	1.23756E-01	2.34990E-03	1.44996E-16	0.165	98.1	3.55363E+01	107.3	1.2
710	25	2.66195E-01	4.20299E-05	1.61808E-16	0.182	100.0	3.53722E+01	106.9	0.7
740	12	4.29593E-01	8.10962E-03	1.15583E-16	0.195	93.3	3.37291E+01	102.0	1.9
740	50	1.37758E-01	4.01085E-04	2.13600E-16	0.218	99.7	3.56146E+01	107.6	1.7
780	12	4.30584E-02	3.82164E-04	8.55806E-17	0.227	99.7	3.75358E+01	113.2	2.7
820	12	4.53827E-01	2.10491E-03	1.63842E-16	0.244	98.4	3.74831E+01	113.0	1.6
860	12	1.61285E-01	2.75702E-03	2.30636E-16	0.269	97.9	3.74009E+01	112.8	0.9
890	12	1.06623E-01	6.93505E-03	2.26010E-16	0.293	94.7	3.70146E+01	111.7	1.4
890	25	1.54159E-01	5.38620E-03	2.17040E-16	0.316	95.8	3.67755E+01	111.0	1.2
920	25	3.47659E-01	9.50465E-03	2.31952E-16	0.341	93.3	3.94819E+01	118.9	2.7
950	25	8.00983E-02	5.36863E-03	2.27760E-16	0.365	96.3	4.13868E+01	124.4	1.5
950	50	1.20322E-01	9.06859E-03	2.75834E-16	0.394	94.0	4.21318E+01	126.6	1.6
975	25	1.25740E-01	5.93850E-03	1.60495E-16	0.411	96.2	4.50364E+01	135.0	2.7
1000	25	3.59806E-01	9.84227E-05	1.98783E-16	0.433	99.9	4.54527E+01	136.2	1.5
1025	25	1.82310E-02	7.82920E-04	2.34881E-16	0.458	99.5	4.80979E+01	143.8	1.1
1050	25	1.57637E-01	5.21288E-03	3.32036E-16	0.493	97.1	5.19879E+01	155.0	0.7
1075	25	1.12275E-02	5.94118E-03	4.54014E-16	0.541	96.9	5.56162E+01	165.3	1.2
1100	25	9.33513E-02	6.45472E-03	6.30831E-16	0.609	96.8	5.76616E+01	171.1	1.1
1100	50	1.82103E-03	2.79989E-03	6.51994E-16	0.678	98.6	5.72746E+01	170.0	1.1
1100	77	1.00485E-01	1.25115E-04	3.25950E-16	0.713	99.9	5.64800E+01	167.7	1.5
1200	12	2.02752E-01	1.57668E-02	3.76553E-16	0.753	93.6	6.83558E+01	201.1	2.1
1260	12	7.42742E-03	4.34587E-03	1.10980E-15	0.871	97.9	6.00381E+01	177.8	1.3
1320	12	1.56179E-02	3.41086E-03	7.40098E-16	0.950	98.0	5.01682E+01	149.8	0.6
1400	12	1.29508E-04	1.65466E-02	2.55423E-16	0.977	91.6	5.36279E+01	159.6	1.3
1500	12	4.83879E-02	6.60285E-04	1.98317E-16	0.998	99.7	5.65496E+01	167.9	1.5
1550	12	2.50289E+00	2.64189E-03	1.62903E-17	1.000	98.6	5.43776E+01	161.8	6.5